



UvA-DARE (Digital Academic Repository)

A "Hyperburst" in the MAXI J0556-332 Neutron Star

Evidence for a New Type of Thermonuclear Explosion

Page, D.; Homan, J.; Nava-Callejas, M.; Cavecchi, Y.; Beznogov, M.V.; Degenaar, N. ; Wijnands, R. ; Parikh, A.S.

DOI

[10.3847/1538-4357/ac72a8](https://doi.org/10.3847/1538-4357/ac72a8)

Publication date

2022

Document Version

Final published version

Published in

Astrophysical Journal

License

CC BY

[Link to publication](#)

Citation for published version (APA):

Page, D., Homan, J., Nava-Callejas, M., Cavecchi, Y., Beznogov, M. V., Degenaar, N., Wijnands, R., & Parikh, A. S. (2022). A "Hyperburst" in the MAXI J0556-332 Neutron Star: Evidence for a New Type of Thermonuclear Explosion. *Astrophysical Journal*, 933(2), [933]. <https://doi.org/10.3847/1538-4357/ac72a8>

General rights

It is not permitted to download or to forward/distribute the text or part of it without the consent of the author(s) and/or copyright holder(s), other than for strictly personal, individual use, unless the work is under an open content license (like Creative Commons).

Disclaimer/Complaints regulations

If you believe that digital publication of certain material infringes any of your rights or (privacy) interests, please let the Library know, stating your reasons. In case of a legitimate complaint, the Library will make the material inaccessible and/or remove it from the website. Please Ask the Library: <https://uba.uva.nl/en/contact>, or a letter to: Library of the University of Amsterdam, Secretariat, Singel 425, 1012 WP Amsterdam, The Netherlands. You will be contacted as soon as possible.

UvA-DARE is a service provided by the library of the University of Amsterdam (<https://dare.uva.nl>)



A “Hyperburst” in the MAXI J0556–332 Neutron Star: Evidence for a New Type of Thermonuclear Explosion

Dany Page¹ , Jeroen Homan² , Martin Nava-Callejas¹ , Yuri Cavecchi¹ , Mikhail V. Beznogov^{1,3} , Nathalie Degenaar⁴ , Rudy Wijnands⁴ , and Aastha S. Parikh⁴

¹ Instituto de Astronomía, Universidad Nacional Autónoma de México, Ciudad de México, CDMX 04510, Mexico; page@astro.unam.mx, ycavecchi@astro.unam.mx, mnavac@astro.unam.mx

² Eureka Scientific, Inc., 2452 Delmer Street, Oakland, CA 94602, USA; jeroenhoman@icloud.com

³ National Institute for Physics and Nuclear Engineering (IFIN-HH), RO-077125 Bucharest, Romania; mikhail.beznogov@nipne.ro

⁴ Anton Pannekoek Institute for Astronomy, University of Amsterdam, Postbus 94249, 1090 GE Amsterdam, The Netherlands; degenaar@uva.nl, r.a.d.wijnands@uva.nl

Received 2022 February 8; revised 2022 May 4; accepted 2022 May 20; published 2022 July 15

Abstract

The study of transiently accreting neutron stars provides a powerful means to elucidate the properties of neutron star crusts. We present extensive numerical simulations of the evolution of the neutron star in the transient low-mass X-ray binary MAXI J0556–332. We model nearly 20 observations obtained during the quiescence phases after four different outbursts of the source in the past decade, considering the heating of the star during accretion by the deep crustal heating mechanism complemented by some shallow heating source. We show that cooling data are consistent with a single source of shallow heating acting during the last three outbursts, while a very different and powerful energy source is required to explain the extremely high effective temperature of the neutron star, ~ 350 eV, when it exited the first observed outburst. We propose that a gigantic thermonuclear explosion, a “hyperburst” from unstable burning of neutron-rich isotopes of oxygen or neon, occurred a few weeks before the end of the first outburst, releasing $\sim 10^{44}$ ergs at densities of the order of 10^{11} g cm⁻³. This would be the first observation of a hyperburst, and these would be extremely rare events, as the buildup of the exploding layer requires about a millennium of accretion history. Despite its large energy output, the hyperburst did not produce, due to its depth, any noticeable increase in luminosity during the accretion phase and is only identifiable by its imprint on the later cooling of the neutron star.

Unified Astronomy Thesaurus concepts: Neutron stars (1108); Accretion (14); Low-mass x-ray binary stars (939); Astrophysical explosive burning (100)

1. Introduction

Observations of the cooling of neutron stars in transient low-mass X-ray binaries after a long phase of accretion have opened a new window in the study of neutron star interiors. During accretion, compression of matter in the neutron star crust induces a series of nonequilibrium reactions, such as electron captures, neutron emissions, and pycnonuclear fusions (Bisnovatyĭ-Kogan & Chechetkin 1979; Sato 1979; Haensel & Zdunik 1990). The energy generated by these reactions slowly diffuses into the neutron star core, a mechanism known as “deep crustal heating” (Brown et al. 1998), which, over a long time, will lead to an equilibrium between this heating and photon and neutrino cooling mechanisms (Miralda-Escude et al. 1990; Brown et al. 1998; Colpi et al. 2001). Depending on the star’s core temperature, the timescale to establish this equilibrium can range from a few decades for an initially very cold core, up to millions of years for the hottest stars (Wijnands et al. 2013). Regarding evolution on short timescales, theoretical modeling found that in the case of a long and strong enough accretion outburst, the crust can be driven out of thermal equilibrium with the core (Rutledge et al. 2002). This led to the prediction that subsequent cooling of the crust (once accretion has stopped and the surface temperature is no longer controlled by the mass accretion but rather by the internal evolution of the star) should be observable on a timescale of a few

years. This prediction has been amply confirmed, and to date crust cooling after an accretion outburst has been observed in almost a dozen cases, which we reproduce in Figure 1.

After observations of the cooling of the first quasi-persistent source that went into quiescence (KS 1731-260; Wijnands et al. 2001; Cackett et al. 2006), theoretical modeling found it was not possible to reproduce the high temperature of the first data point, obtained two months after the end of the outburst, within the deep crustal heating scenario (Shternin et al. 2007). The introduction of another energy source, located at low densities and dubbed “shallow heating,” was found to be necessary in the models (Brown & Cumming 2009). The deep crustal heating generates an energy Q_{dc} of about 1.5–2 MeV per accreted nucleon (Gupta et al. 2008; Haensel & Zdunik 2008; Fantina et al. 2018; Shchegilin et al. 2021), most of it through pycnonuclear fusions in the inner crust at densities above 10^{12} g cm⁻³. In contrast, shallow heating has been found to deposit energy at densities well below 10^{11} g cm⁻³, but its strength, Q_{sh} , as well as the depth at which it is deposited, appear to vary significantly from one source to another. Typical values needed for Q_{sh} are of the order of 1–3 MeV. However, in some cases (XTE J1701-462; Page & Reddy 2013; and Swift J174805.3-244637; Degenaar et al. 2015), it was not found to be required, while in the case of MAXI J0556–332 (Deibel et al. 2015), it could be well above 10 MeV.

1.1. MAXI J0556–332

In the present work, we focus on the thermal evolution of the neutron star in MAXI J0556–332, an X-ray transient that was



Original content from this work may be used under the terms of the [Creative Commons Attribution 4.0 licence](https://creativecommons.org/licenses/by/4.0/). Any further distribution of this work must maintain attribution to the author(s) and the title of the work, journal citation and DOI.

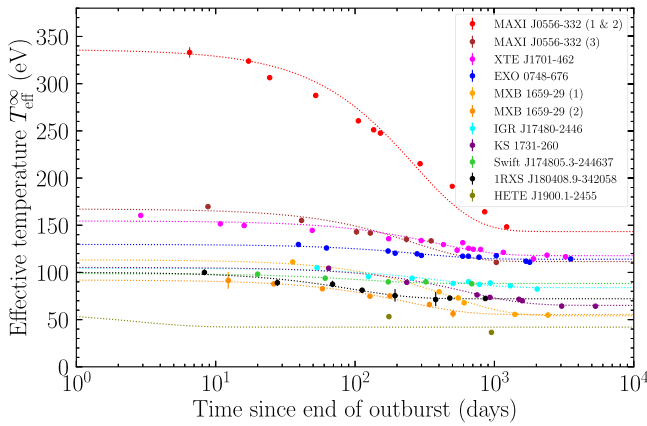


Figure 1. Present sample of cooling observations after long accretion outbursts from the sources: MAXI J0556–332 outbursts 1 and 2 together (outburst 2 was small and had almost no effect on the cooling curve: see Figure 6 below) and 3 (Parikh et al. 2017a; this work), XTE J1701–462 (Parikh et al. 2020), EXO 0748–676 (Parikh et al. 2020), two outbursts from MXB 1659–29 (Parikh et al. 2019), IGR J17480–2446 (Ootes et al. 2019), KS 1731–260 (Merritt et al. 2016), Swift J174805.3–244637 (Degenaar et al. 2015), 1RXS J180408.9–342058 (Parikh et al. 2017b, 2018), and HETE J1900.1–2455 (Degenaar et al. 2021). Dotted lines show simple fits of the form $T(t) = T_{\infty} + \Delta T \exp(-t/\tau)$ to guide the eye and have no claim to be physically meaningful.

discovered in early 2011 (Matsumura et al. 2011) when it had started a major outburst. It was in outburst for 16 months before it returned to quiescence in 2012 May. Although no thermonuclear bursts or pulsations were detected, the behavior of the source in an X-ray hardness–intensity diagram strongly suggested that the accreting compact object in MAXI J0556–332 is a neutron star: the tracks traced out at the highest fluxes showed a strong resemblance to those of the most luminous neutron star low-mass X-ray binaries, the Z sources. Based on a flux comparison with other Z sources, Homan et al. (2011) suggested that the source is a very distant halo source.

MAXI J0556–332 has shown three smaller outbursts since its discovery outburst, in late 2012, 2016, and 2020. Homan et al. (2014) studied the cooling of the neutron star after the first two outbursts. They found that during the first few years in quiescence after the 2011/2012 outburst, the neutron star in MAXI J0556–332 was exceptionally hot compared to the other cooling neutron stars that have been studied, as can be seen in Figure 1. The smaller second outburst that started in late 2012 and lasted ~ 115 days did not produce detectable deviations from the cooling trend seen after the first outburst. Deibel et al. (2015) showed that to produce the extremely high temperatures observed after the first outburst, a high amount of shallow heating was required (~ 6 – 16 MeV per accreted nucleon). They further concluded that the shallow heating mechanism did not operate during the second outburst. Parikh et al. (2017a) analyzed the neutron star cooling observed after the first three outbursts. Reheating of the crust was observed after the third outburst. It was concluded that the strength of the shallow heating in MAXI J0556–332 varied from outburst to outburst. For two other sources, the cooling has been studied after multiple outbursts as well. In MXB 1659–29, the strength of the shallow heating was found to be constant in the two outbursts after which cooling was studied. For Aql X-1, with numerous but short outbursts, the shallow heating was found to differ in both strength and depth between outbursts (Degenaar et al. 2019). A definitive explanation for a varying shallow

heating in MAXI J0556–332 and Aql X-1 has not been provided yet.

Here we present a re-modeling of the crustal cooling data of MAXI J0556–332, including data taken after the end of the most recent outburst from 2020. We argue that the high crustal temperatures caused by the 2011/2012 outbursts were not the result of anomalously strong shallow heating, but were instead caused by a gigantic thermonuclear explosion that occurred at some time during the last three weeks of that outburst. As this explosion was much more energetic than any other thermonuclear X-ray burst observed to date, even about 100 times more powerful than a superburst, we find it appropriate to call it a “hyperburst.” We infer it must have been produced by unstable thermonuclear burning of neutron-rich isotopes of oxygen or neon.

The paper is organized as follows. In Section 2 we present the analysis of the data taken during and soon after the 2020 outburst of MAXI J0556–332. In Section 3 we briefly describe how we model the neutron star temperature evolution, and in Section 4 we compare two different scenarios of shallow heating. In Section 5 we propose the new scenario of a hyperburst as the cause of the hot crust of MAXI J0556–332 when it exited the first 2011–2012 observed outburst, and in Section 6 we try to identify the source of this explosion. We discuss our results in Section 7 and conclude in Section 8.

2. The 2020 Accretion Outburst

2.1. NICER Observations

The 2020 outburst of MAXI J0556–332 was monitored extensively with the X-ray Timing Instrument (XTI) on board the Neutron Star Interior Composition Explorer (NICER; Gendreau et al. 2016). The XTI provides coverage in the 0.2–12 keV band and consists of 56 nonimaging X-ray concentrators that are coupled to focal plane modules (FPMs), each containing a silicon drift detector. At the time of the observations, 52 of the 56 FPMs were functional. A total of 107 ObsIDs are available for the 2020 outburst, each with one or more good-time intervals (GTIs). Data were reprocessed with the `nicerl2` tool that is part of HEASOFT v6.29. Default filtering criteria⁵ were used. We additionally used the count rate in the 13–15 keV band, where no source contribution is expected, to filter out episodes of increased background (13–15 keV count rates > 1.0 counts s^{-1} per 52 FPMs). After filtering, a total exposure of ~ 332 ks remained.

A full 0.5–10 keV outburst light curve was made with one data point per GTI. The GTIs varied in length from 16 s to ~ 2.1 ks. The outburst light curve is shown in Figure 2(a). NICER observations started 6 days after the first MAXI/GSC detection of source activity (Negoro et al. 2020; see orange dashed line in Figure 2) and caught the source during a fast rise toward the peak of the outburst. After the peak of the outburst, the NICER count rate dropped rapidly for ~ 20 days, after which the count rate decreased more slowly until the end of the outburst, about half a year later.

We also produced 0.5–10 keV light curves for each ObsID with a time resolution of 1 s to search for possible X-ray bursts. One candidate X-ray burst was found in ObsID 3201400198 (MJD 59147, 2020 October 25). A segment of the light curve of the observation is shown in Figure 3. The burst is very short

⁵ https://heasarc.gsfc.nasa.gov/docs/nicer/analysis_threads/nicerl2/

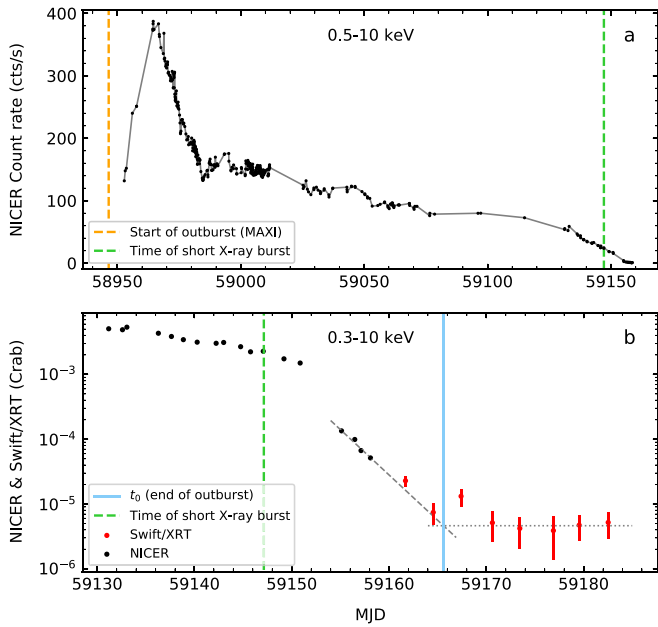


Figure 2. (a): NICER 0.5–10 keV light curve of the 2020 outburst of MAXI J0556–332. Each data point represents a single GTI. Background was not subtracted. The start of the outburst (as observed with MAXI) and the occurrence of a small X-ray burst are marked with the dashed orange and green lines, respectively. (b) NICER (black) and Swift (red) coverage of the decay into quiescence. Each data point represents the background-subtracted 0.3–10 keV count rate in Crab units. The blue line shows the estimate of the end of the outburst (MJD 59165.6), obtained by finding the intersection between an exponential fit to the last four NICER and first two Swift data points, and a constant fit to the last five Swift data points.

(<10 s from start to end) and peaks at a count rate a factor ~ 3 higher than the persistent emission. Fits to the spectrum of the persistent emission slightly favor a soft spectral state at the time of the burst. Fitting a “double-thermal” model (Lin et al. 2007) with n_{H} fixed to $3.2 \times 10^{20} \text{ cm}^{-2}$ (Parikh et al. 2017b) gives blackbody and disk-blackbody temperatures of 1.45(1) keV and 0.42(1), respectively, with a reduced χ^2 of 1.00 (a typical hard state model, blackbody with power law, resulted in a slightly worse reduced χ^2 of 1.07). The unabsorbed 0.5–10 keV flux was $5.8 \times 10^{-11} \text{ erg cm}^{-2} \text{ s}^{-1}$, corresponding to a luminosity of $1.3 \times 10^{37} \text{ erg s}^{-1}$ for a distance of 43.6 kpc (Parikh et al. 2017b). Careful inspection of the data suggests that the burst is not the result of a short, sudden increase in the background. The burst is also present in various subsets of detectors, indicating that the burst was not instrumental. The count rates during the burst are too low to perform a study of the spectral evolution, but the burst was more pronounced at higher energies ($>2 \text{ keV}$), which is consistent with a thermonuclear (type I) X-ray burst. We used WebPIMMS⁶ to convert the peak count rate (75 counts s^{-1}) into a 0.01–100 keV luminosity (assuming a blackbody temperature of 2.5 keV, a distance of 43.6 kpc, and an n_{H} of $3.2 \times 10^{20} \text{ cm}^{-2}$): $\sim 3.8 \times 10^{38} \text{ erg s}^{-1}$, which is very close to the empirical Eddington limit of neutron stars (Kuulkers et al. 2003). This would constitute the first detection of a type I X-ray burst from MAXI J0556–332 and would add further proof that the compact object is a neutron star.

Background-subtracted spectra were produced for each ObsID using the `nicerbackgen3C50` tool (Remillard

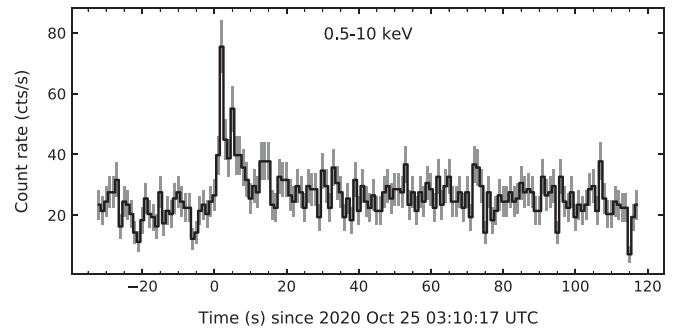


Figure 3. A 0.5–10 keV light curve of MAXI J0556–332 (ObsID 3201400198) showing a short X-ray burst. The time resolution is 1 s.

et al. 2022), which uses several empirical parameters to construct background spectra from a library of observations of NICER background fields. FPMs 14 and 34 were excluded, since they tend to be affected by noise more often than the other detectors. We note that background spectra could only be extracted for 76 of the 107 ObsIDs; for the remaining ones, the empirical parameters fell outside the range covered by the library background observations. From the resulting spectra, a background-subtracted 0.3–10 keV light curve was produced. In Section 2.2 this light curve will be used in conjunction with Swift data to estimate the end of the outburst and the start of quiescence.

2.2. Swift Observations

The Neil Gehrels Swift Observatory X-Ray Telescope (Swift-XRT; Burrows et al. 2005) observed MAXI J0556–332 eight times near the end of the 2020 outburst. A 0.3–10 keV light curve with one data point per ObsID was produced by the online Swift-XRT products generator⁷ (Evans et al. 2007, 2009). Background was not subtracted, since the corrections were expected to be only minor ($\sim 5\%$). The Swift light curve (red data points) is shown together with the NICER background-subtracted data (black) in Figure 2(b). Both the Swift and NICER data were normalized to Crab units.

The NICER data in Figure 2(b) cover a switch from a slow to a rapid decay, around MJD 59153. The Swift data covered the end of the decay and the start of quiescence, as indicated by the leveling off of the count rates. To estimate the start of quiescence (t_0), we determined the intersection of the decay (modeled with an exponential) and the quiescent level (modeled with a constant). A similar method was previously employed for other sources (see Fridriksson et al. 2010; Waterhouse et al. 2016; Parikh et al. 2017b, 2019). The exponential fit was made to the last four NICER and the first two Swift data points. The constant fit was made to the last five Swift data points. The third Swift data point was excluded since the higher count rate indicated a possible short episode of enhanced accretion, which was also observed several times soon after the end of the 2011/2012 outburst (Homan et al. 2014). From the fits, we find $t_0 = \text{MJD } 59165.6$. This time is marked with a blue line in Figure 2(b), along with the exponential (dashed line) and constant fits (dotted line).

Again using the online Swift-XRT products generator, we extracted a single background-subtracted quiescent spectrum for the last five Swift observations. The spectrum had an exposure time of $\sim 12.6 \text{ ks}$, contained ~ 30 counts, and was fit

⁶ <https://heasarc.gsfc.nasa.gov/cgi-bin/Tools/w3pimms/w3pimms.pl>

⁷ https://www.swift.ac.uk/user_objects/

with XSPEC v12.12 (Arnaud 1996) using C-statistics. We used a similar absorbed neutron star atmosphere model as in Homan et al. (2014) and Parikh et al. (2017a): `constant×tbabs×nsa`. Note that these authors employed `nsa` instead of the frequently used neutron star atmosphere model `nsatmos` (Heinke et al. 2006), since the latter model does not allow temperatures above $\log_{10}(kT) = 6.5$. `constant` is set to a value of 0.92 to account for cross-calibration with other X-ray detectors. Although only a Swift spectrum is analyzed in our work, the n_{H} and distance used in our fits are based on the Chandra and XMM-Newton spectra fitted by Parikh et al. (2017a); not using the cross-calibration constant would result in a temperature that is too low. The absorption component `tbabs` is an updated version of the `tbnew_feo` component used by Homan et al. (2014), but it yields the same column densities. We set the abundances to `WILM` and cross sections to `VERN`, and fixed the n_{H} to the value obtained by Parikh et al. (2017a): $3.2 \times 10^{20} \text{ cm}^{-2}$. For the neutron star atmosphere component `nsa`, we fixed the neutron star mass (M) and radius⁸ (R) to $1.4 M_{\odot}$ and 10 km, respectively, and for the normalization, we used a distance of 43.6 kpc. The only free parameter in the fit was the temperature of the `nsa` component. When converted to the effective temperature measured at infinity,⁹ we find a value of $166 \pm 8 \text{ eV}$. This data point (for which we use the midpoint of the five observations as date: MJD 59176.6) was added to the cooling data obtained by Parikh et al. (2017a) from prior Swift, Chandra, and XMM-Newton observations.

2.3. 2019 XMM-Newton Observation

An XMM-Newton observation of MAXI J0556–332 was made in 2019 that was not included in the set of observations presented in Parikh et al. (2017a). The observation (0824730201) was performed from 2019 February 11–12 and was analyzed using the XMM-Newton Science Analysis System version 16.0.0, following the steps outlined in Section 2.4 of Parikh et al. (2017a). After the filtering, we obtained the following exposure times for the three European Photo Imaging Cameras (EPIC): 67.7 ks (pn), 91.8 ks (MOS1), and 96.1 ks (MOS2). Using the same fitting model as for the Swift spectrum, we obtained an effective temperature measured at infinity of $110.4 \pm 1.4 \text{ eV}$. For the date, we used the midpoint of the observation: MJD 58525.3.

3. Modeling the Evolution of the MAXI J0556–332 Neutron Star

We build on our previous experience in modeling accretion heated neutron stars using an updated version of the code `NSCOOL` (Page 2016), which solves the general relativistic equations of stellar structure and thermal evolution. The physics we employ is standard and briefly described in Appendix A.

To model the mass accretion rate during the four observed outbursts, we apply a similar method as previously described in Ootes et al. (2016, 2018) and Parikh et al. (2017a). However, instead of using a mix of Swift, NICER, and MAXI data to estimate the evolution of the bolometric flux, we opt to only use the MAXI data, since they provide a single consistent set that covers all four outbursts and requires just one count-rate-

to-flux conversion factor. For the 2–20 keV MAXI count rate to bolometric flux conversion factor, we used the value from Parikh et al. (2017a): $2.353 \times 10^{-8} \text{ erg cm}^{-2} \text{ count}^{-1}$.

From the bolometric flux F_{bol} , we calculate the daily average mass accretion rate using

$$\dot{M} = \frac{F_{\text{bol}} 4\pi D^2}{\eta c^2} \quad (1)$$

where D is the source distance, fixed here at $D = 43.6 \text{ kpc}$, c is the speed of light, and $\eta \approx 0.2$ is the accretion efficiency factor (Shapiro & Teukolsky 1983). Heating was assumed to only take place during the outburst intervals, which were fixed by hand and are shown as gray shaded areas in Figure 6. The temporal evolution of the heating luminosities, $H_{\text{dc}}(t)$ for the deep crustal heating and $H_{\text{sh}}(t)$ for the shallow heating, follow the instantaneous mass accretion rate as

$$\begin{pmatrix} H_{\text{dc}}(t) \\ H_{\text{sh}}(t) \end{pmatrix} = \begin{pmatrix} Q_{\text{dc}} \\ Q_{\text{sh}} \end{pmatrix} \times \frac{\dot{M}(t)}{m_u} \quad (2)$$

with their respective strengths Q_{dc} and Q_{sh} . We follow Haensel & Zdunik (2008) and use $Q_{\text{dc}} = 1.93 \text{ MeV}$, which is distributed in density at the locations of each reaction (see Figure 3 in Haensel & Zdunik 2008) for the model starting with ^{56}Fe at low densities. For the shallow heating, we assume Q_{sh} is distributed uniformly, per unit volume, within a shell covering a density range from ρ_{sh} up to $5\rho_{\text{sh}}$. Details of the distribution of Q_{sh} in this narrow shell as, e.g., uniform distribution per unit mass instead of per unit volume, are of little relevance since the injected heat has enough time to diffuse within the shell during the outbursts. Both Q_{sh} and ρ_{sh} are considered, in a purely phenomenological manner, as free parameters that are adjusted to fit the data.

In our model of a thermonuclear hyperburst, we assume that an energy $X_{\text{hb}} \times 10^{18} \text{ erg g}^{-1}$ is deposited almost instantaneously at time t_{hb} in a shell going from our outer boundary layer (at $\rho = \rho_b = 10^8 \text{ g cm}^{-3}$) up to a density ρ_{hb} . We envision the layer at density ρ_{hb} as a “critical layer” and this density as a “critical density,” being the point where the hyperburst is triggered. The temperature of this critical layer at the moment when the hyperburst is triggered, T_{hb} , is not fixed in any way but will be an output of our simulations and will be referred to as a “critical temperature.” X_{hb} , t_{hb} , and ρ_{hb} are also treated phenomenologically as free parameters to fit the data. An energy of $10^{18} \text{ erg g}^{-1}$ corresponds to about 1 MeV per nucleon and is a typical energy released by fusion of C, O, or Ne into iron-peak nuclei so that X_{hb} roughly represents the mass fraction of the exploding nuclear species.

In the previous study of the evolution of MAXI J0556–332 in Parikh et al. (2017a), a χ^2 minimization technique was used to obtain the best fit to the data. Here, however, we apply the more robust method, for models with many parameters, of Markov Chain Monte Carlo (MCMC) using our recently developed MCMC driver `MXMX` (see Lin et al. 2018; Ootes et al. 2019; Degenaar et al. 2021). The parameters we vary are the mass M and radius R of the star (which, among other properties¹⁰, determine the crust thickness which is a dominant

⁸ In this paper, by “radius” we always mean the coordinate radius in Schwarzschild coordinates, i.e., *not* the “radius at infinity.”

⁹ $T_{\text{eff}}^{\infty} = T_{\text{eff}}/(1+z)$, where $(1+z) \equiv (1 - R_S/R)^{-1/2}$ is the gravitational redshift factor, with $R_S = 2GM/c^2$ being the Schwarzschild radius.

¹⁰ Notice that our spectral fits to deduce T_{eff} were performed assuming $M = 1.4 M_{\odot}$ and $R = 10 \text{ km}$: for full consistency with our MCMC runs, these should be performed for a range of M and R . These, we expect, would result in shifts of T_{eff} of the order of 10% and should not have a major impact on our conclusions.

factor in controlling, on one hand, the timescale for heat transport and, on the other hand, the amount of matter present and thus the amount of energy needed to heat it), the initial redshifted core temperature \tilde{T}_0 , the depth of the light element layer in the stellar envelope, y_L (which affects the observed effective temperature T_{eff}), the impurity parameter Q_{imp} (which can strongly reduce the thermal conductivity in the solid crust), the strength and depth of the shallow heating, Q_{sh} and ρ_{sh} , and, when considered, the properties of the hyperburst, X_{hb} , t_{hb} , and ρ_{hb} . In Appendix B we describe the various settings we apply in the various scenarios presented in the following sections.

4. Shallow Heating in the Four Observed Accretion Outbursts

To extend the work of Parikh et al. (2017a) and incorporate the new information from the 2020 accretion outburst, we set up a first scenario, “A,” with 20 parameters: M , R , \tilde{T}_0 , five zones with different $Q_{\text{imp}}^{(i)}$ ($i = 1, \dots, 5$), and, for each one of the four observed accretion outbursts $y_L^{(j)}$, $Q_{\text{sh}}^{(j)}$, and $\rho_{\text{sh}}^{(j)}$ ($j = 1, \dots, 4$). We allow $Q_{\text{sh}}^{(1)}$ to take values up to 20 MeV while we restrict $Q_{\text{sh}}^{(2),(3),(4)}$ to at most 1 MeV in light of the results of Parikh et al. (2017a). In all cases, $\log_{10} \rho_{\text{sh}}^{(j)}$ can take any value between 8.2 and 10.2 (in g cm^{-3}). Under these premises, we ran our MCMC (see Appendix B for details) and generated about 2 million samples. We present in Figure 4 (continuous lines) the posterior distribution of the eight parameters $Q_{\text{sh}}^{(j)}$ and $\rho_{\text{sh}}^{(j)}$. There is a clear dichotomy between outburst 1 on one hand and the next three ones on the other hand, already clearly identified by Deibel et al. (2015) and Parikh et al. (2017a), with $Q_{\text{sh}}^{(1)} \geq 10$ MeV while $Q_{\text{sh}}^{(2,3,4)} \leq 1$ MeV. Notice that the values of $Q_{\text{sh}}^{(1)}$ show no upper limit because, as found by Deibel et al. (2015), when it is far above 10 MeV, the outer crust becomes so hot that most of the shallow heating energy is lost to neutrinos. Increasing $Q_{\text{sh}}^{(1)}$ has no further effect on the temperature profile so that an arbitrary cutoff has to be introduced (we choose 20 MeV). However, the distributions of both $Q_{\text{sh}}^{(j)}$ and $\log_{10} \rho_{\text{sh}}^{(j)}$ in outbursts 2, 3, and 4 point to the possibility that shallow heating had the same properties in these three outbursts. To evaluate this possibility, we consider a second scenario, “B,” in which $Q_{\text{sh}}^{(j)}$ and $\rho_{\text{sh}}^{(j)}$ have the same values in these three outbursts, $Q_{\text{sh}}^{(j)} = Q_{\text{sh}}^{(234)}$ and $\rho_{\text{sh}}^{(j)} = \rho_{\text{sh}}^{(234)}$ for $j = 2, 3$, and 4. The resulting posterior distributions, from a second MCMC run (see Appendix B for details) that also generated about 2 million samples, are plotted in Figure 4 as dotted lines. To compare these two scenarios, we plot in Figure 5 the resulting χ^2 distributions. It is clear that there is no really significant difference between them, and considering that scenario “B” has 16 parameters versus 20 in scenario “A,” it seems there is no gain in considering that the shallow heating had different properties in the last three outbursts. (Scenario “C” is described in Section 5.)

It is important to notice that in scenario “B,” the distribution of $Q_{\text{sh}}^{(234)}$ is essentially determined by the third outburst in which both scenarios result in the same posterior distribution. Hopefully further observations of the relaxation of MAXI J0556–332 in the near future will more strongly constrain the properties of shallow heating in the fourth outburst and strengthen our present conclusion that data from outbursts 2, 3, and 4 are compatible with having identical Q_{sh} and ρ_{sh} .

5. A Gigantic Thermonuclear Explosion in the First Accretion Outburst

Having shown that modeling outbursts 2, 3, and 4 with identical shallow heating parameters leads to an equally good fit to the data as having different parameters in each outburst, we now postulate that during the first 2011–2012 outburst, shallow heating was of the same kind as in the next three outbursts, i.e., also describable with the same parameters, and that the extremely high temperature of the neutron star at the end of that outburst is due to another phenomenon. We explore here the possibility that this event may have been a gigantic thermonuclear explosion, triggered deep in the outer crust. We, thus, present a third scenario, “C,” with a single parameterization of the shallow heating, Q_{sh} and ρ_{sh} , operating in all four accretion outbursts and add a sudden heat injection with parameters X_{hb} , t_{hb} , and ρ_{hb} , as presented in Section 3, with t_{hb} adjustable to any time during the first outburst, whose duration was 1.31 yr, and ρ_{hb} allowed to take values between 10^8 up to 10^{12} g cm^{-3} and X_{hb} in the range 0–0.05.

To explore scenario “C,” we ran our MCMC again (see Appendix B for details), and in Figure 5 the resulting distribution of the χ^2 of this scenario is also exhibited. There is no significant difference between the χ^2 of the three scenarios; “A” and “C” have slightly larger distributions below 20, but this could simply reflect the fact they have more parameters than “B” (20 and 17 versus 16, respectively). This simple comparison indicates that scenario C appears statistically at least as good as the first two.

In Figure 6 we illustrate in detail one of the good models found in this manner. The two upper panels display the overall evolution of both the daily mass accretion rate \dot{M} and the star’s redshifted effective temperature T_{eff}^∞ , while the four central ones exhibit an excellent fit to the 19 data points that we obtained after more than a decade long evolution. In the lower-left panel of Figure 6, one can see the constant rise in the temperature at the bottom of the exploding layer, at density ρ_{hb} , which could be consistent with this temperature reaching a critical value at which some nuclear burning becomes unstable resulting in a thermonuclear runaway. We attempt to identify the fuel of the explosion in the next section. In the lower-right panel, we present the temperature profile in the whole star at the time just before the explosion, compared with a model where shallow heating was not implemented, showing that the occurrence of shallow heating was crucial in setting this profile in the outer crust. In Figure 7 we detail the evolution of the internal temperature, before (left panel) and after (right panel) the hyperburst starting from the beginning of the first accretion outburst, at time t_{start} . The profile at 48 days corresponds to the highest temperature in the region where the shallow heating is operating and is occurring when the mass accretion rate is at its maximum. In the subsequent profiles, one can notice the decreasing temperature of this low-density region due to both the decrease of the mass accretion rate and the flow of heat inward, the latter resulting in a rising temperature in the density range 10^{10} – 10^{12} g cm^{-3} . This explains the constant temperature rise at the point where the explosion will be triggered, at $\rho_{\text{hb}} = 10^{11}$ g cm^{-3} , as seen in the lower-left panel of Figure 6. Notice that in the low-density layers, due to their low heat capacity and resulting short thermal timescales, the temperature follows the variations of the mass accretion and heating rates. At higher densities, the heating has a more cumulative effect, and the temperature keeps rising while the mass accretion rate

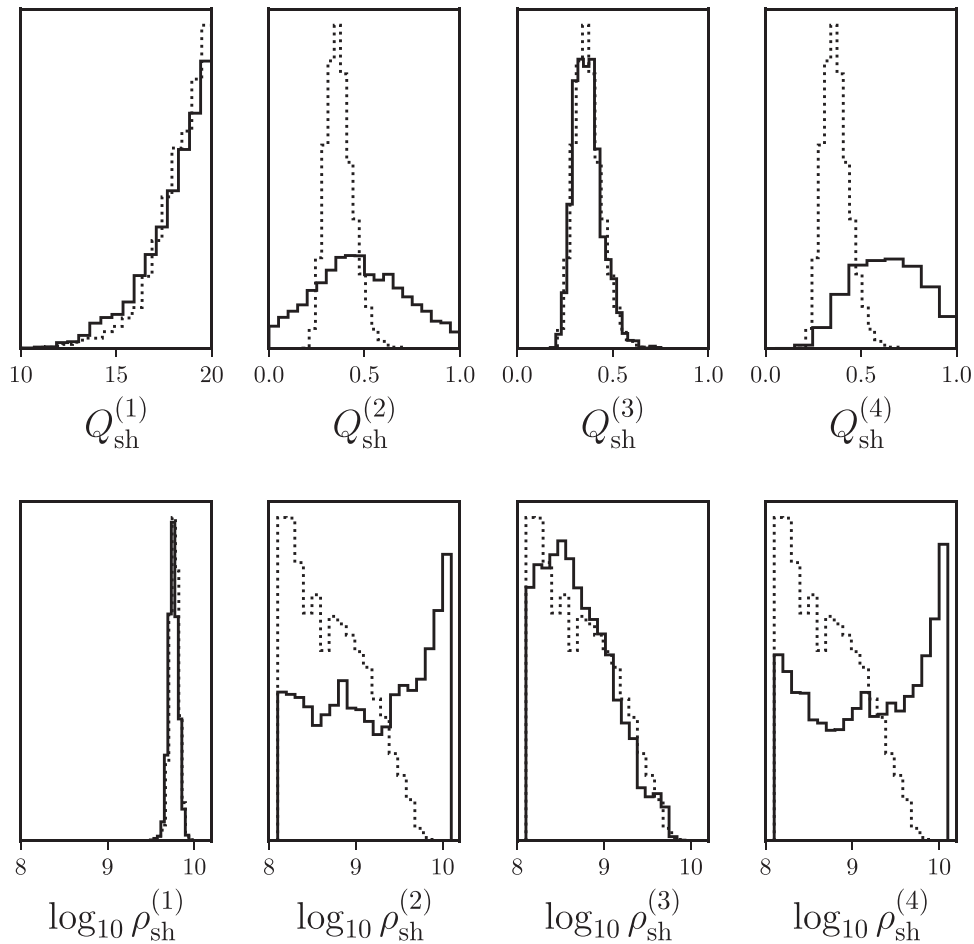


Figure 4. Histograms of the posterior distributions of the strength, $Q_{\text{sh}}^{(i)}$ in MeV, and lower density, $\rho_{\text{sh}}^{(i)}$ in g cm^{-3} , of shallow heating during outburst i ($i = 1, \dots, 4$) for Scenario “A,” continuous lines, and “B,” dotted lines. (Vertical scales are linear and adjusted such that the two histograms cover the same area.)

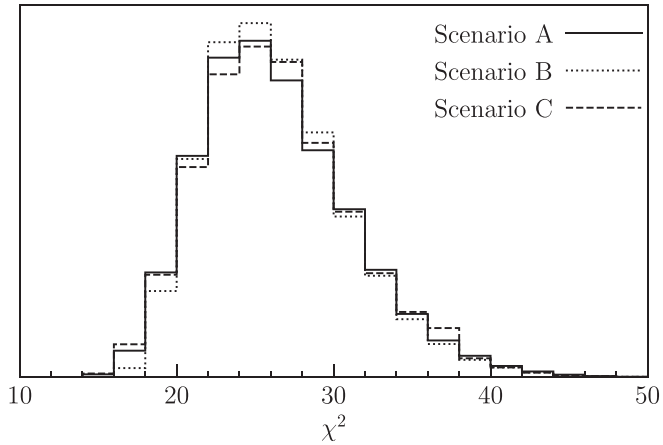


Figure 5. Histograms comparing the χ^2 distributions of our three scenarios “A,” “B,” and “C.” We have about 2 million samples in scenarios “A” and “B” and 4 million in “C.”

decreases (a similar evolution can be clearly seen in the “Supporting Information” movie of Ootes et al. 2016). The right panel of Figure 7 illustrates the relaxation of the temperature after the heat injection from the hyperburst: due to a fixed energy injection per gram, the initial profile peaks at the highest density ρ_{hb} . The initial rapid drop in temperature is due to neutrino losses (Deibel et al. 2015), and during the relaxation under accretion, i.e., at t before t_0 , the peak moves

back toward the shallow heating region. After the end of the accretion, the absence of heating and the heat flow toward the surface result in the maximum temperature peak moving toward higher densities. As a result of the inward heat flow, a large part of the energy released by the explosion is being stored at higher densities and will result in a very long cooling time. One can see in the “Cooling curve” panel of Figure 6 that even after the perturbation from the third outburst, the cooling trajectory is a continuation of the trajectory from the first outburst (Parikh et al. 2017a).

The global energetics of scenario “C” resulting from our MCMC are presented in Figure 8. We find that a typical hyperburst energy E_{hb} is of the order of 10^{44} ergs, which is about two orders of magnitude larger than that of a superburst (Cumming et al. 2006) and is comparable to the energy output of a magnetar giant flare (Kaspi & Beloborodov 2017). However, the total energy injected into the star from both the shallow and the deep crustal heating, E_{h} , is larger than E_{hb} by a factor of a few, and the energy lost through photon emission, E_{γ} , is of comparable magnitude. In most cases, however, E_{γ} is somewhat smaller than the total heating energy $E_{\text{hb}} + E_{\text{h}}$. The energy not lost to photons is stored into the core, and neutrino losses will contribute to the global energy balance in the long term (Brown et al. 1998; Colpi et al. 2001); however, a detailed study of this issue is beyond the scope of the present work. Finally, the rightmost panel of Figure 8 shows the distribution of the peak luminosity $L_{\gamma \text{ max}}$ coming from the stellar interior

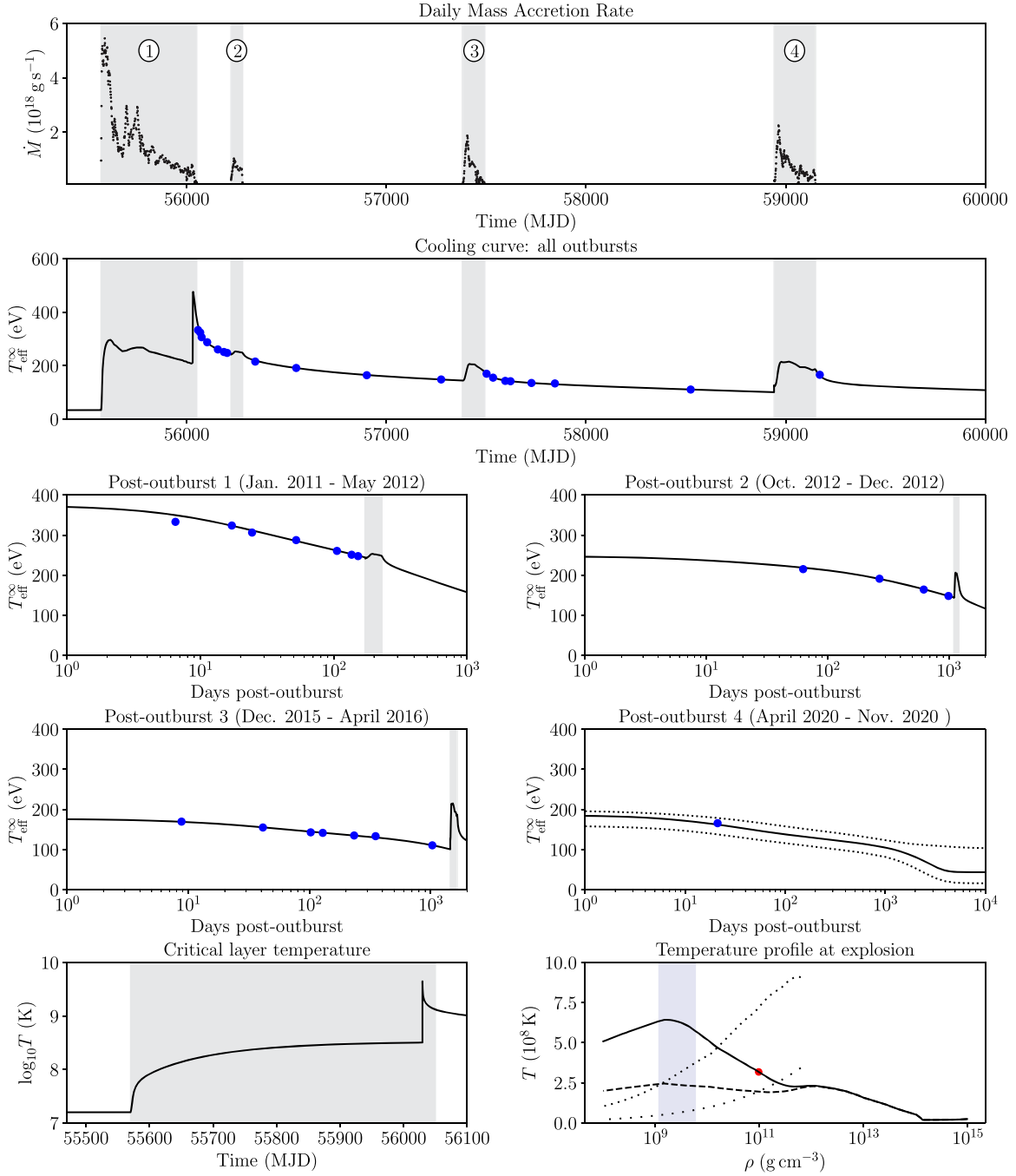


Figure 6. Evolution of a $1.6 M_{\odot}$ model, with a radius of 11.2 km and an initial redshifted core temperature $\bar{T}_0 = 1.2 \times 10^7$ K. Its shallow heating parameters are $Q_{\text{sh}} = 0.390$ MeV distributed in the density range $[1.15 - 5.7] \times 10^9 \text{ g cm}^{-3}$. The two upper panels show the whole temporal evolution, spanning more than 10 yr and four accretion outbursts, of the daily mass accretion rate, \dot{M} , and redshifted effective temperature, T_{eff}^{∞} , while the four central panels show details of the relaxation after each accretion outburst. (In parentheses are the initial and final dates of the outburst.) With 19 measurements of T_{eff}^{∞} , this model has a χ^2 of 24.6. In all of these panels, the gray shaded areas delineate the periods of accretion. In the “Post-outburst 4” panel, the two dotted lines show the 3σ range of predictions from the whole set of our scenario “C” models. The lower-left panel displays the evolution of the local temperature in the critical layer at density $\rho_{\text{hb}} = 10^{11} \text{ g cm}^{-3}$ during the first accretion outburst where the hyperburst occurred at time of 56030 MJD, i.e., three weeks before the end of the outburst. The lower-right panel displays the local temperature profile in the whole star (continuous line) just before the time when the hyperburst was triggered, where the red dot signals the position of the critical layer at ρ_{hb} , and the dashed curve shows the temperature profile at the same time in the absence of shallow heating. The blue shaded density range shows the region where the shallow heating is assumed to take place. The dotted curves show the melting temperature of the main matter (upper dotted curve) and of ^{26}Ne bubbles in pressure equilibrium with the main matter (lower dotted curve).

during the hyperburst that is radiated as photons from the surface. Unfortunately this luminosity $L_{\gamma \text{ max}}$ is always significantly smaller than the X-ray luminosity inferred from the observed flux, $\sim 10^{38} \text{ erg s}^{-1}$ for a distance of 43.6 kpc as we assume here, and thus unlikely to be noticeable in the data.

However, since we do not model the explosion at low densities (our outer boundary being at density $\rho_b = 10^8 \text{ g cm}^{-3}$), we cannot exclude that a hyperburst may trigger a lower-density X-ray burst, in a manner similar to the superburst precursors (see, e.g., Galloway & Keek 2021), which could be detectable.

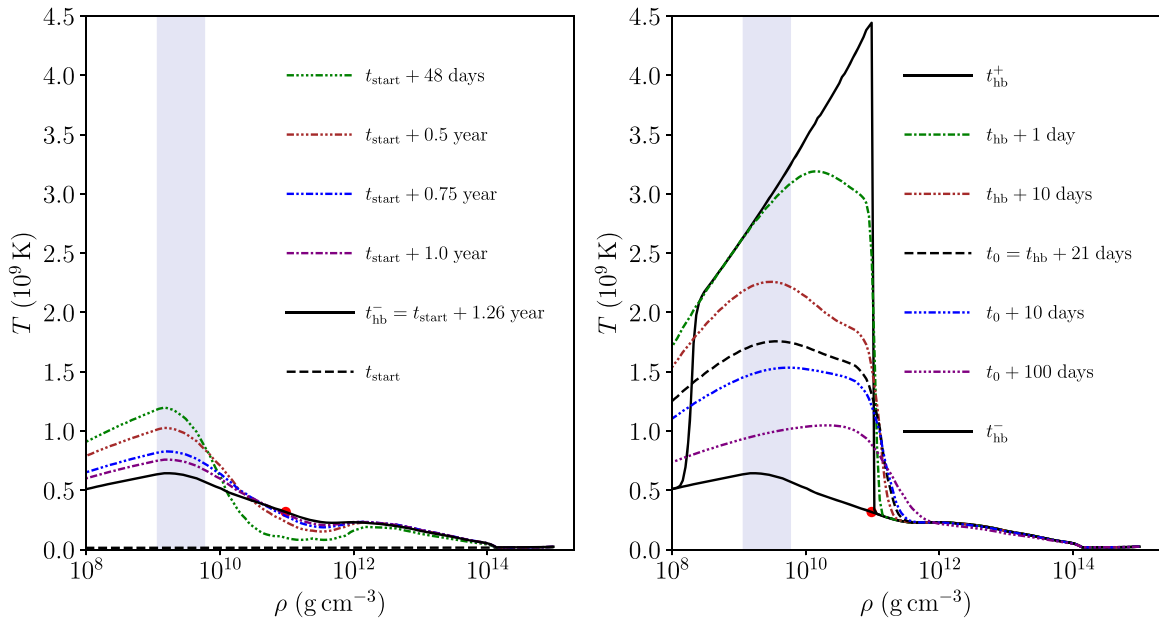


Figure 7. Evolution of the neutron star internal temperature profile for the same model as in Figure 6. Left panel: profiles starting at the beginning of the first accretion outburst, t_{start} , and five posterior times until just before the hyperburst explosion, t_{hb}^- . Right panel: profiles starting just before, t_{hb}^- , and after, t_{hb}^+ , the hyperburst explosion, with three posterior times until the end of the accretion outburst, t_0 , and two later times during the quiescent phase. In both panels, the blue shaded region marks the density range where the shallow heating is operating (during accretion). (Numerically, the hyperburst energy is smoothly injected over 200 s, the actual time interval from t_{hb}^- to t_{hb}^+ . Moreover, no energy is injected close to the outer boundary at 10^8 g cm^{-3} , but this anomaly is corrected by diffusion in less than a day as seen from the $t_{\text{hb}} + 1$ day profile.)

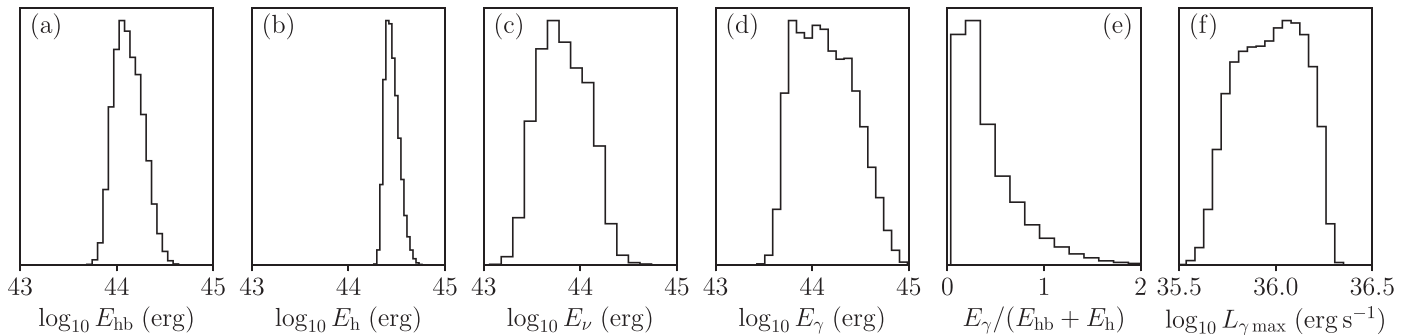


Figure 8. Histograms of the distributions of some results from our scenario “C” MCMC: (a) total hyperburst energy, E_{hb} , (b) total heating (shallow + deep crust), E_{h} , during the four outbursts, total energy lost to (c) neutrinos, E_{ν} , and (d) photons, E_{γ} , from the beginning of the first outburst until the end of the fourth one. Panel (e) shows the ratio of energy lost through photon emission to the total injected energy $E_{\text{hb}} + E_{\text{h}}$. The last panel, (f), shows the histogram of the maximum luminosity coming out of the stellar interior during the hyperburst.

We also show in Figure 9 the posterior distribution of the strength, Q_{sh} , and lower density, ρ_{sh} , of the shallow heating in our scenario “C.” The Q_{sh} distribution peaks at 0.6 MeV, which is slightly higher than in scenario “B” where the peak was at 0.4 MeV. As in scenario “B,” the distribution of ρ_{sh} is leaning on its lower permitted value. Exploring this peak at lower densities would, however, imply lowering the outer boundary density of our models in NSCOO1 and require a significant extension of the code’s numerics that will be implemented in a future paper.¹¹

We emphasize that the MCMC process was driven to fit the data using, as parameters for the hyperburst, only its occurrence time, t_{hb} , depth, ρ_{hb} , and total energy, through X_{hb} . We made no further assumption about the nature of the explosion, its fuel, and the temperature at which it was triggered. To characterize the

physical conditions of the hyperburst trigger, we display in Figure 10 a summary of the most important results of this scenario “C.” Besides the posterior distribution of five of our most relevant MCMC parameters, we also report the posterior distribution of two quantities that are output of our calculation: (1) the temperature of the critical layer just before ignition, T_{hb} , and (2) the cooling sensitivity (Equations (4) and (3)), which will be of interest in Section 6. The first noticeable result is a slightly bimodal distribution in terms of mass and radius: the dominant peak is located at $\sim (2M_{\odot}, 10.5 \text{ km})$, and the second smaller one around $\sim (1.5M_{\odot}, 12.5 \text{ km})$. These peaks also exhibit clear differences in critical density and temperature. For the first quantity, there is a threshold at $10^{11} \text{ g cm}^{-3}$ above (below) which the dominant (lower) peak can be found, while for the latter quantity, their respective temperatures are $\sim 10^{8.6} \approx 4 \times 10^8 \text{ K}$ for the dominant and $\sim 10^{8.4} \approx 2.5 \times 10^8 \text{ K}$ for the lower one. Also of relevance is the fact that the dominant peak favors a trigger time t_{hb} very close to the end of the accretion outburst, while the second peak favors $t_{\text{hb}} \simeq 1.25 \text{ yr}$, i.e., about 25 days before the

¹¹ Such an extension has been performed (Beznogov et al. 2020), but the resulting code is too slow to be employed in massive calculations as in an MCMC.

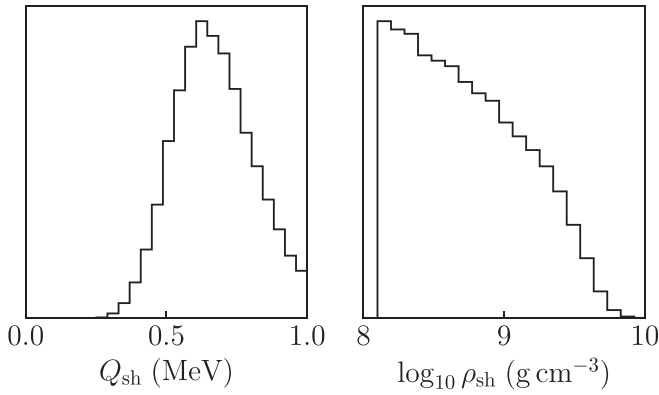


Figure 9. Histograms of the distribution of the shallow heating strength, Q_{sh} , and lower density, ρ_{sh} in scenario “C.”

end of the outburst. Notice, finally, that the column density y_{hb} corresponding to ρ_{hb} has a narrow, symmetric distribution centered at $10^{15} \text{ g cm}^{-2}$. (The column density y is defined as $dy = -\rho dr$, and is related to the pressure through $P = yg_s$ in the outer layers where the gravitational acceleration g can be approximated by its surface value $g_s = GM/R^2/\sqrt{1 - 2GM/Rc^2}$.)

6. The Fuel of the Hyperburst

In the classical short H/He X-ray bursts, as well as the long C superbursts, matter in the stellar envelope is pushed by accretion toward higher densities and temperatures until it reaches a critical point where the nuclear burning becomes unstable and a thermonuclear explosion ensues. The timescale for this compression is hours to days in the case of the short bursts and months to years for the superbursts. In our scenario, an explosion is triggered at densities $\sim 10^{11} \text{ g cm}^{-3}$, corresponding to column densities of the order of $10^{15} \text{ g cm}^{-2}$. Under an Eddington accretion rate ($\dot{m}_{\text{Edd}} \approx 10^5 \text{ g cm}^{-2} \text{ s}^{-1}$), at such densities matter is barely progressing by one millimeter per day, and the timescale to reach this point is centuries to millennia. Moreover, matter is being pushed toward lower temperatures because of the inverted temperature gradient (lower-right panel of Figure 6). However, we are not in a steady-state situation but rather in a 1.5 yr long strong outburst during which the critical layer is still warming up (lower-left panel of Figure 6 and left panel of Figure 7). The physical origin of the explosion thus appears to be the result of the temperature at the critical layer rising with time rather than this matter being pushed toward higher densities.

A standard criterion in X-ray burst modeling to identify the location of the ignition layer (Fujimoto et al. 1981; Fushiki & Lamb 1987; Bildsten et al. 1998) is to compare the temperature sensitivity of the nuclear burning rate, $\varepsilon_{\text{nucl}}$, with that of the cooling rate

$$\varepsilon_{\text{cool}} \equiv \frac{\partial F}{\partial y} = -\frac{1}{\rho} \frac{\partial F}{\partial r}, \quad (3)$$

where F is the heat flux. As long as the inequality

$$\frac{\delta \varepsilon_{\text{cool}}}{\delta T} > \frac{\delta \varepsilon_{\text{nucl}}}{\delta T} = \frac{d \varepsilon_{\text{nucl}}}{dT} \quad (4)$$

is satisfied, the burning is considered to be stable. Notice that $\varepsilon_{\text{cool}}$ is a nonlocal quantity as it contains the second derivative

of T versus r and depends on the whole T -profile: its derivative in the left-hand side of Equation (4) is a functional derivative with respect to some perturbation $\delta T(y)$. A discussion of various possible estimates of the functional derivative $\delta \varepsilon_{\text{cool}}/\delta T$ was presented by Potekhin & Chabrier (2012). Of primary importance is the length scale over which $\delta T(y)$ can be estimated to be significantly altered. For such a typical length scale, we will consider the temperature scale height, H_T , defined through

$$\frac{dT}{dr} = \frac{T}{H_T} \quad (5)$$

so that the flux is simply $F = -KT/H_T$, where K is the thermal conductivity. We then employ the estimate

$$\varepsilon_{\text{cool}} \simeq \frac{KT}{\rho H_T^2} \quad (6)$$

and deduce

$$\frac{\delta \varepsilon_{\text{cool}}}{\delta T} \sim \frac{K}{\rho H_T^2} \quad (7)$$

where we neglected the temperature dependence of K , a good approximation since, in the $\rho - T$ range where the explosion occurs, ions form a classical solid in which K is only very weakly T -dependent (Yakovlev & Urpin 1980). (General relativistic corrections are neglected in these approximate expressions.) We have explicitly checked that more involved schemes result in values differing only by factors of a few that have negligible impact on our results, in agreement with the discussion of Potekhin & Chabrier (2012). Histograms of the values of $\log_{10} \delta \varepsilon_{\text{cool}}/\delta T$, calculated on the temperature profile of each model at ρ_{hb} just before the time t_{hb} , were presented in Figure 10. We found that triggering of the hyperburst occurred at values $\log_{10} \delta \varepsilon_{\text{cool}}/\delta T \sim -2$ to -1 (with $\varepsilon_{\text{cool}}$ in $\text{erg g}^{-1} \text{ s}^{-1}$ and T in K). In contradistinction, $\varepsilon_{\text{nucl}}$ depends only on the value of T at the point under consideration so that the right-hand side of Equation (4) is a simple normal derivative. We do not include neutrino cooling in our estimates as ε_{ν} is several orders of magnitude smaller than the diffusive $\varepsilon_{\text{cool}}$ of Equation (6) in the (ρ, T) region we are interested in.

The candidate nucleus to trigger the hyperburst must have been produced by nuclear burning, either stable or explosive, at lower densities and then pushed to high densities by accretion. On its journey, this nucleus will have undergone electron captures as described, e.g., by Haensel & Zdunik (1990). The most abundant light nuclei produced by the nuclear burning in the envelope are α -nuclei, and in Figure 11 we show how the six lightest ones (excluding ${}^8\text{Be}$, which is unstable) evolved under double electron captures when pushed to increasing densities. These are our pre-candidates for the triggering of the hyperburst.

One interesting feature of the physical conditions where the hyperburst is triggered, which may affect the conclusions about the triggering species, is that the crust main matter, in the temperature and density ranges where the explosion starts, is in a solid (likely crystallized) state: the lower-right panel of Figure 6 displays the melting temperature curve of the main matter, which shows that on this temperature profile, solidification occurs close to $10^{10} \text{ g cm}^{-3}$. However, it has

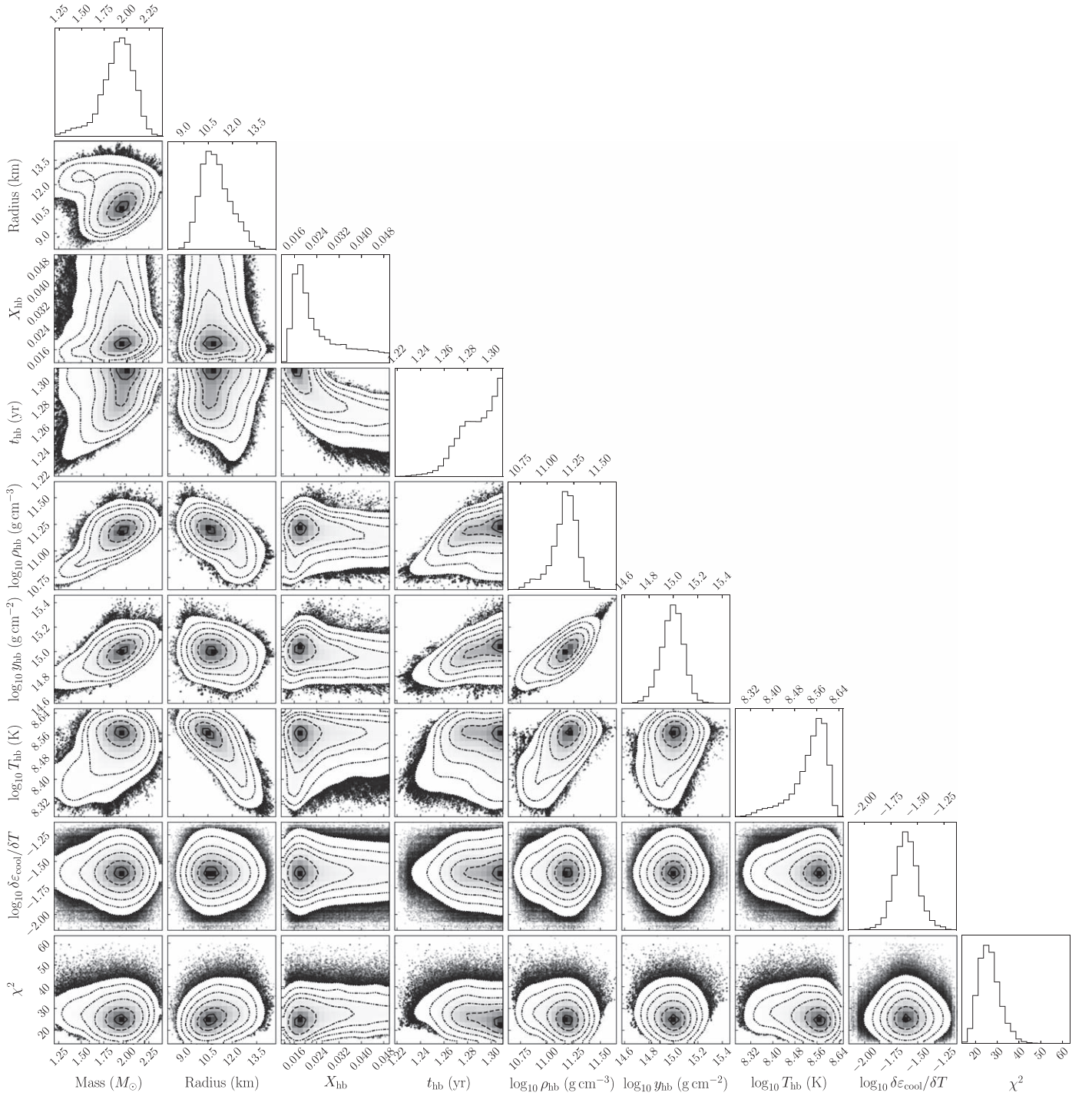


Figure 10. Corner plot of 1D and 2D histograms of the posterior distributions of five MCMC parameters, mass and radius of the model, and the three hyperburst control parameters, X_{hb} , t_{hb} , and ρ_{hb} , as well as its equivalent column density y_{hb} , and two deduced quantities, the critical temperature, T_{hb} , and the cooling sensitivity, $\log_{10} \delta \epsilon_{\text{cool}} / \delta T$ (see Equations (4) and (3) with ϵ_{cool} measured in $\text{erg g}^{-1} \text{s}^{-1}$ and T in K.), calculated at the critical density at time t_{hb} , as well as the χ^2 of the model fit to the 19 data points.

been predicted (Horowitz et al. 2007) that when the high Z nuclei solidify, there is a phase separation with the low Z ones that remain in the liquid phase. The emerging state could thus be one of bubbles of liquid O and/or Ne embedded in a solid medium. We also display in the lower-right panel of Figure 6 the melting temperature for ^{28}Ne bubbles in these conditions, which shows that they remain in a liquid state, given this temperature profile, up to densities well above $10^{11} \text{ g cm}^{-3}$.

Oxygen bubbles have even lower melting temperatures than neon ones because of their lower Z .

In Figure 12 we present the critical conditions for the burning of α -nuclei with $Z = 6, 8,$ and 10 (details are presented in Appendix D) in the $\rho - T$ plane where the $1\sigma, 2\sigma,$ and 3σ critical confidence regions for the values of $(\rho_{\text{hb}}, T_{\text{hb}})$ from Figure 10 are shown in the background. In the upper panels, we plot contour lines of $\log_{10} d\epsilon_{\text{nuc}}/dT = -2$. In the lower panels,

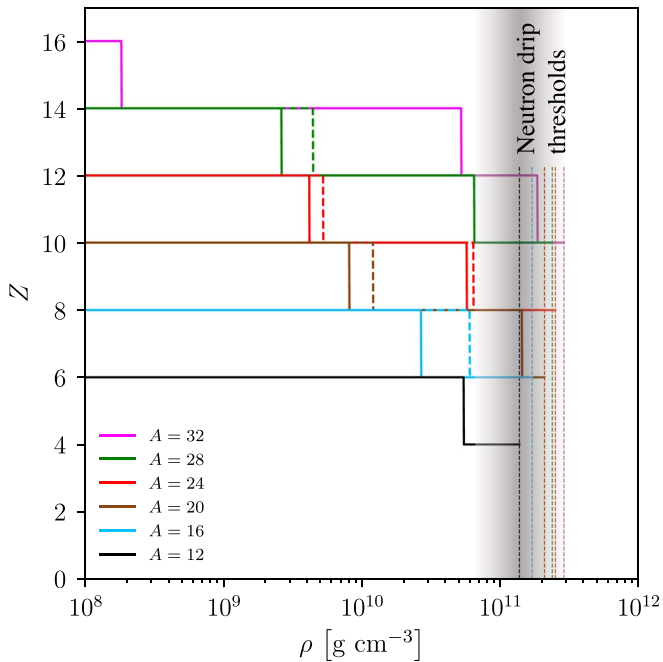


Figure 11. Evolution of the charge number Z , under the effect of double electron captures, of the six lightest α -nuclei, ^{12}C , ^{16}O , ^{20}Ne , ^{24}Mg , ^{28}Si , and ^{32}S , from their production site, at densities below 10^9 g cm^{-3} , when pushed to increasing densities. Continuous lines allow forbidden electron captures, while dashed lines only consider allowed transitions. Vertical dotted lines show the neutron drip density thresholds for each isobaric sequence. The gray shaded region corresponds to the predicted location of the origin of the hyperburst, and in this density range, excluding or including forbidden transitions makes no difference. Details of the calculation are provided in Appendix C.

we plot contour lines of the lifetimes $\tau = 1000 \text{ yr}$ of the same nuclei, since 1000 yr is a typical time for matter to be pushed to these densities by accretion. Even if the medium average mass fraction $\langle X \rangle$ of the triggering nucleus is small, its mass fraction in the bubbles where it is concentrated during medium crystallization (if concentration did occur) could be close to unity. To encompass this range of possibilities, all critical contour lines in Figure 12 consider a range of X from 10^{-6} (no bubble formation) up to unity (perfect bubble formation). Depending on the actual mass fraction of the possible exploding nuclei, we have a variation of a factor of a few in the predicted density where the explosion started. At these densities, and relatively low temperatures, uncertainties on the burning rates are largely dominated by uncertainties in the screening, and we apply either the estimated minimum rates, in the left panels, or the maximum ones, in the right panels. Notice that the burning rates depend strongly on the charge number, Z , of the nuclei and have much less sensitivity to their mass number, A , so that considering different isotopes has little impact on this part of our inquiry. From Figure 12 we see that carbon is unlikely to be the trigger nucleus of our hyperburst (it is most likely the trigger nucleus of superbursts acting at lower densities $\sim 10^9 \text{ g cm}^{-3}$; Cumming & Bildsten 2001 and Cumming et al. 2006). It is only at very low concentrations, $X < 10^{-6}$, that carbon burning can be unstable within the critical region of the $\rho - T$ plane. Oxygen appears to be the best candidate, but neon cannot be excluded particularly if actual reaction rates are close to the maximum value we apply, and the hyperburst critical density is on the high end values found by the MCMC. Oxygen could be ^{20}O coming from ^{20}Ne after a pair of electron captures or ^{24}O coming from ^{24}Mg after two

pairs of electron captures, as pictured in Figure 11. Similarly, neon could be ^{28}Ne coming from ^{28}Si or ^{32}Ne coming from ^{32}S .

The lower panels of Figure 12 show that both oxygen and neon nuclei need to be pushed to densities higher than their explosion densities before they are exhausted and, thus, exhaustion by stable burning is not an issue.

As a last point, we compare the temperature dependence of $\varepsilon_{\text{nucl}}$, i.e., $\nu = d \ln \varepsilon_{\text{nucl}} / d \ln T$ so that locally $\varepsilon_{\text{nucl}} \propto T^\nu$, with that of $\varepsilon_{\text{cool}}$, the latter being $\varepsilon_{\text{cool}} \propto T$ in the regime of interest, as seen from Equation (6). Several typical values of ν are marked on the contours of Figure 12. In the case of minimum reaction rate (left panels) over the entire 3σ range of (ρ, T) where the explosion is predicted to have occurred, we find that $\nu \geq 10 \gg 1 \sim \delta \ln \varepsilon_{\text{cool}} / \delta \ln T$ so that $\varepsilon_{\text{nucl}}$ is clearly much more sensitive to temperature variations than $\varepsilon_{\text{cool}}$, in agreement with the idea of a thermonuclear explosion. However, in the case of maximum rate (right panels) in a large part of the 3σ range of (ρ, T) , $\nu \ll 1$, indicating an almost purely pycnonuclear burning, which makes it doubtful a successful explosion may occur in these conditions. It is only in the highest range of T that $\nu \gg 1$ in both the oxygen and neon cases, neon burning exhibiting larger values of ν , and thus it is a more likely trigger nucleus in this case.

7. Discussion

Now having data for a fourth outburst in MAXI J0556–332, our first finding is that shallow heating of the neutron star during outbursts 2, 3, and 4 can be described by identical parameters, Q_{sh} and ρ_{sh} (see Equation (2) and the description following it). The thermal evolution of this neutron star when exiting its first outburst implies, however, a very different physical condition, as is easily intuited by a look at Figure 1. Such a condition had previously been described as an extremely strong continuous shallow heating, with $Q_{\text{sh}} \sim 10\text{--}20 \text{ MeV}$ compared to $\sim 1 \text{ MeV}$ in outbursts 2 and 3 (Deibel et al. 2015; Parikh et al. 2017a).

Our second finding is that the high temperature of the MAXI J0556–332 neutron star when exiting outburst 1 (as well as its subsequent years-long thermal evolution) can be very well modeled assuming a very strong and sudden energy release—a “hyperburst,” instead of a continuous energy release, as in the shallow heating scenario. From our extensive MCMC simulation, scenario “C,” we find that this event would have occurred during the last 3 weeks of the accretion outburst and released an energy of the order of 10^{44} ergs. In this scenario, the energy was deposited in a layer extending from the lowest density up to $\sim 10^{11} \text{ g cm}^{-3}$: global energetics as well as other characteristics are presented in Figures 8 and 10. Shallow heating was also assumed to occur during the first outburst, and described by the same parameters as in the next three outbursts (see Figure 9 for the parameter posterior distributions).

In the presence of shallow heating, there is a natural break in the cooling curve, occurring during the first few weeks, which is determined by the depth of the energy source as described by Deibel et al. (2015). In the case of MAXI J0556–332, such a break is seen in the cooling data after the first outburst, comparing the first two points at days 6 and 17 with the following ones: this break is reproducible within the shallow heating scenario (Deibel et al. 2015), and its presence determines the narrowness of the $\rho_{\text{sh}}^{(1)}$ distribution peak (see Figure 4). No such break is seen in the cooling data of the other three outbursts, implying, within the shallow heating scenario,

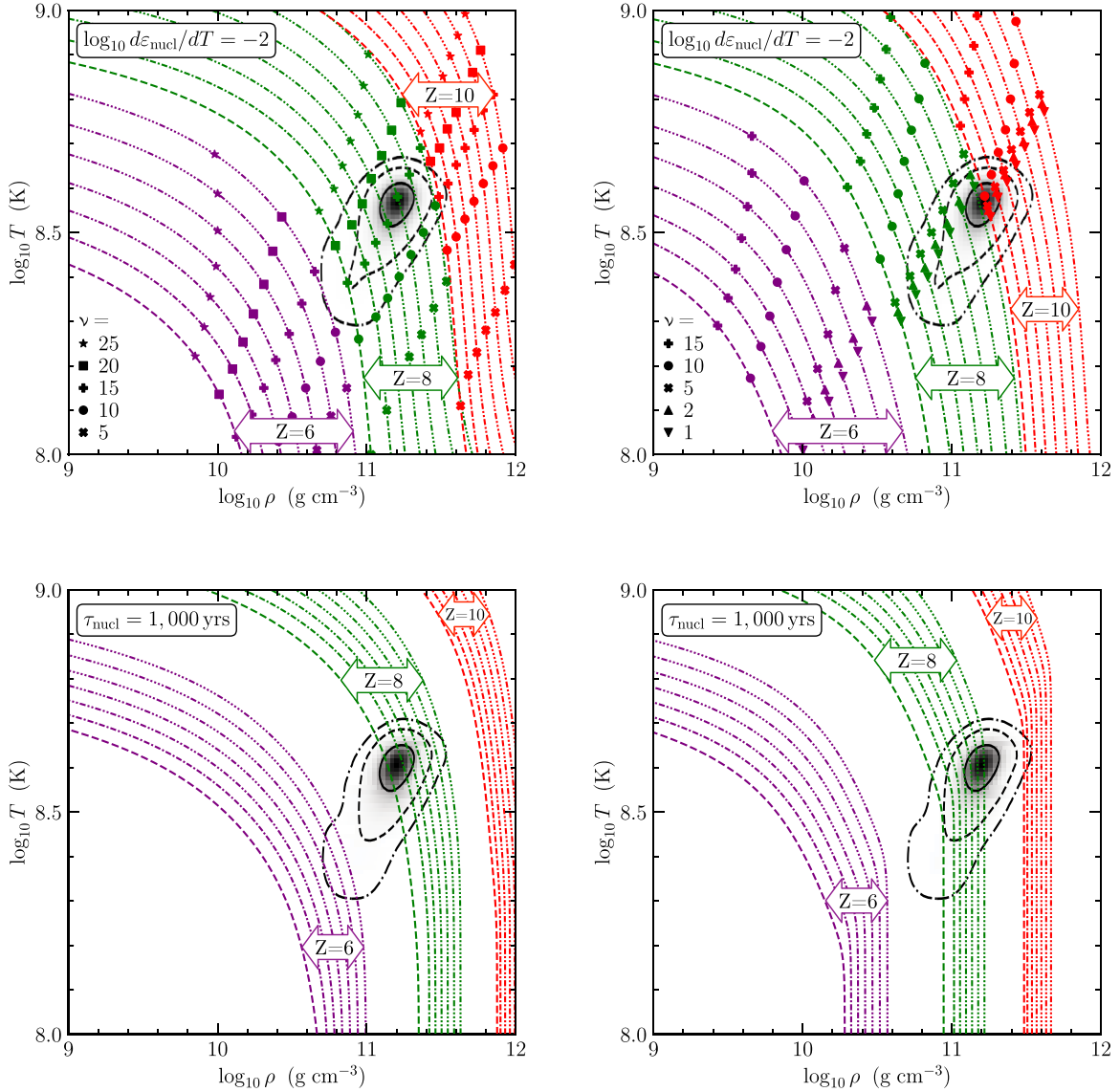


Figure 12. Upper panels: contour lines where $\log_{10} d\epsilon_{\text{nucl}}/dT = -2$ (ϵ_{nucl} being in $\text{erg g}^{-1} \text{s}^{-1}$ and T in K) for the fusion of $^{16}\text{C}+^{16}\text{C}$ (labeled “ $Z = 6$ ”), $^{20}\text{O}+^{20}\text{O}$ (labeled “ $Z = 8$ ”), and $^{28}\text{Ne}+^{28}\text{Ne}$ (labeled “ $Z = 10$ ”), and for each case with seven mass fractions $X = 10^{-n}$ with $n = 0, 1, 2, \dots, 6$, as dashed- (n) -dotted lines. Symbols on the contour lines mark points where $\nu = d \ln \epsilon_{\text{nucl}} / d \ln T$ reaches some specific values: these are 5, 10, 15, 20, and 25 in the left panels and 1, 2, 5, 10, and 15 in the right panels. Lower panels: contour lines of lifetime $\tau = 10^3$ yr of the ^{16}C , ^{20}O , and ^{28}Ne nuclei under the same fusion reactions as in the upper panels. For the treatment of screening, these nuclei are assumed to be immersed in a background of ^{56}Ca , with mass fraction $1 - X$, which is the nuclear species predicted to be present at $\rho \sim 10^{11} \text{ g cm}^{-3}$ in the model of Haensel & Zdenik (2008). In the left panels, we apply the minimum reaction rates, while in the right panels, the maximum ones are used. Details of the calculations are presented in Appendix D. In all panels, the background contours reproduce the $1\sigma, 2\sigma,$ and 3σ , confidence ranges of the 2D distribution of $\log_{10} \rho_{\text{hb}} - \log_{10} T_{\text{hb}}$ already displayed in Figure 10.

that it must have occurred before the first post-outburst observation. As a result, $\rho_{\text{sh}}^{(2,3,4)}$ in scenario “A” are not as precisely determined as $\rho_{\text{sh}}^{(1)}$, and their posterior distributions are very broad. Within the hyperburst scenario, however, since the effect of the shallow heating is completely dominated by the effect of the hyperburst, no model exhibits such a break after the first outburst and is, thus, able to perfectly fit the first data point after outburst 1. The “Post-outburst 1” panel of Figure 6 is a typical example of such behavior. Not being able to fit the first observational data point at day 6 after the first outburst may be seen as an argument against the hyperburst scenario, but it is only based on one data point.

To identify candidates for the triggering of the hyperburst, we simply applied the standard criterion of Equation (4) within

the approximation of Equation (7). Values of H_T and $\delta\epsilon_{\text{cool}}/\delta T$ were obtained directly from the T -profile in each one of the models of our MCMC, and we found that $\log_{10} \delta\epsilon_{\text{cool}}/\delta T \sim -2$ to -1 (see Figure 10; with ϵ_{cool} measured in $\text{erg g}^{-1} \text{s}^{-1}$ and T in K). Values of $\log_{10} d\epsilon_{\text{nucl}}/dT = -2$ were calculated and displayed in the two upper panels of Figure 12. Considering the enormous uncertainties on the fusion rate due to screening in, and near to, the pycnonuclear regime, the upper-left panel employed minimum rates, and the upper-right panel used maximum ones. The lower panels of the same figure show “exhaustion lines,” i.e., contour lines where the burning timescale is 1000 yr, implying that the described nucleus would be depleted by stable burning when reaching the corresponding density since 1000 yr is roughly the time it takes, under MAXI J0556–332’s average mass accretion rate,

for matter to reach $10^{11} \text{ g cm}^{-3}$. The conclusion of this is that C is unlikely to be the triggering nucleus, leaving O and Ne as the best candidates.

Isotopes of O and Ne have slightly different burning rates, but the differences are small enough that the results of Figure 12 are practically only dependent on the charge Z of the nucleus and not on their mass number A . Once produced at low densities, nuclei are compressed by accretion and undergo double electron capture reactions that gradually reduce their charge Z (see Figure 11) but without changing the mass A . The triggering oxygen is likely ^{20}O or even ^{24}O , descendants of ^{20}Ne and ^{24}Mg , while the triggering neon would be ^{28}Ne or ^{32}Ne , descendants of ^{28}Si and ^{32}S . When considering the temperature dependence ν of ϵ_{nucl} , we see that in the case of the maximum rate (upper-right panel of Figure 12), most of the MCMC inferred 3σ range in the (ρ, T) plane falls in the pycnonuclear regime in which an explosion is very unlikely, and it is only at the highest inferred temperatures that ν is large enough to make explosive burning possible. In the opposite case of the minimum rate (upper-left panel of Figure 12), $\nu \gg 10$ over the entire inferred (ρ, T) 3σ range, and explosive burning is possible.

Fusion of low Z nuclei liberates about 1 MeV per nucleon, i.e., about $10^{18} \text{ erg g}^{-1}$, and we parameterized the energy injected during the explosion as $X_{\text{hb}} \times 10^{18} \text{ erg g}^{-1}$ so that X_{hb} approximately reflects the average mass fraction, $\langle X \rangle$, of the exploding nuclei. Our MCMC found a peak at $X_{\text{hb}} \sim 0.02$, exhibited in Figure 10, while the minimum value found was 0.011. Thus, a small mass fraction of a few percent of low Z nuclei is needed to provide the required energy. While accretion is ongoing, in the upper layers of the accreted material, H burns into He through the hot CNO cycle and He into C through the triple- α reaction. At high accretion rates, as is the case in MAXI J0556–332, breakout reactions from the CNO cycle add the rp-process (Wallace & Woosley 1981) to H burning and lead to the production of high Z nuclei, possibly up to the SnSbTe cycle at $Z = 50\text{--}52$ and $A = 103\text{--}107$ (Schatz et al. 2001). In the absence of X-ray bursts, the models of Schatz et al. (1999), with continuous burning in the ocean at accretion rates $\sim \dot{M}_{\text{Edd}}$, produced $A = 12$ nuclei at a mass fraction $\sim 4\%$ and $A = 24$ at $\sim 2\%\text{--}3\%$ with other low A nuclei in much smaller abundances and heavy nuclei up to $A \sim 80$ through the rp-process. This is likely representative of the burning in most of the observed accretion phases of MAXI J0556–332 that were close to \dot{M}_{Edd} most of the time (see, e.g., the upper panel of Figure 6) as explosive burning is quenched at high mass accretion rates (e.g., Bildsten et al. 1998; Galloway & Keek 2021). However, during low mass accretion moments, as, e.g., toward the end of an accretion outburst, bursting behavior may appear as was observed in the case of the end of the outburst of XTE J1701-462 when \dot{M} was down to about $10\% \dot{M}_{\text{Edd}}$ (Lin et al. 2009). We notice that MAXI J0556–332’s first outburst, in 2011–2012, was almost a carbon copy of XTE J1701-462’s 2006–2007 outburst; but, nevertheless, no X-ray bursts were detected. Note that we may have found a small X-ray burst toward the end of the 2020 outburst as presented in Section 2.1. Within this context of bursting behavior, we can consider the ashes of the three cases used by Lau et al. (2018): in the extreme rp-process X-ray burst case (based on Schatz et al. 2001), one finds negligible amounts of C and O left but about 1% of $A = 20$ nuclei, while in their KEPLER X-ray burst case (based on Cyburt et al. 2016), one

has to go up to $A = 28$ and 32 to find nuclei with a significant mass fraction, about 5% and 10%, respectively. In both cases, we have enough seed nuclei, which, after multiple double electron captures when pushed to high densities, could be the trigger nuclei for a hyperburst. The third case we contemplate is the occurrence of a superburst (made possible, e.g., by C ashes from long-term continuous burning as seen above). The resulting ashes (based on Keek & Heger 2011) contain negligible amount of C, O, and Ne, but almost 1% of $A = 28$ nuclei, which could lead to a seed nucleus for hyperburst triggering after electron captures. Since the hyperburst is triggered at densities $\sim 10^{11} \text{ g cm}^{-3}$, a region whose chemical composition is the result of many centuries of accretion (of which we only have a decade long snapshot), all of the above burning possibilities may be partial realities and show that having $\sim 1\%\text{--}3\%$ of low Z nuclei present at such densities is a realistic possibility.

We see from Figure 10 that values of the column density at the explosion point, y_{hb} , range from 5×10^{14} up to $2 \times 10^{15} \text{ g cm}^{-2}$. Under an Eddington rate, it takes then approximately from 150 to 600 yr, respectively, of continuous accretion for matter to be pushed to the explosion point. From MAXI J0556–332’s inferred bolometric flux and Equation (1), we deduce a total accreted mass, in the four observed outbursts, of almost 10^{26} g resulting in a 10 yr average $\langle \dot{M} \rangle \simeq 2.8 \times 10^{17} \text{ g s}^{-1} \simeq 4.4 \times 10^{-9} M_{\odot} \text{ yr}^{-1}$, i.e., about 30% of the Eddington rate. Since MAXI J0556–332 was never seen previously to its 2011–2012 outburst, the long-term actual fraction of time it spends in quiescence is possibly much larger than indicated by the last decade of observations, and its long-term $\langle \dot{M} \rangle$ may be smaller than that estimated above. Hyperbursts in MAXI J0556–332 are thus likely once-in-a-few-millennia events, and the probability to have witnessed one in 10 yr since its discovery, or in 25 yr of having continuous all sky monitoring in X-rays, is of the order of 1%: a small but not too small value. The seven known persistent Z sources (Hasinger & van der Klis 1989; Fridriksson et al. 2015), also estimated to be accreting close to, or above, the Eddington limit most of the time, are likely to experience hyperbursts more frequently, once every few centuries. Unfortunately though, these are not detectable under continuous accretion due to the small increase in surface luminosity during the explosion (see panel (f) in Figure 8). From what we found in the present work, a hyperburst can only be recognized if accretion stops shortly afterwards and we detect an anomalously hot neutron star. It could be considered too much of a coincidence that the hyperburst needs to have occurred only a few days/weeks before the end of the outburst. Notice, however, that even if it had happened several months earlier, the star would still have exited the outburst with a very high effective temperature and allowed for the identification of the occurrence of the hyperburst. Figure 1 shows that it took more than 100 days after the end of the outburst, i.e., after the occurrence of the hyperburst, for the crust to cool down and T_{eff}^{∞} to drop below 250 eV. Had the hyperburst occurred 3–4 months before the end of the outburst, the star would have entered quiescence with a temperature in excess of 250 eV, which would already have singled out the MAXI J0556–332 neutron star as an anomalously hot one. At least in the case of MAXI J0556–332, nature appears to have been cooperating!

We now have a handful of binary systems under transient accretion in which post-outburst cooling data are available.

Most of them have much lower mass accretion rates than MAXI J0556–332, which implies that their crusts experience lower temperatures and that their matter would need to be compressed to still higher densities for a hyperburst to be triggered. Hyperbursts in these system are, thus, even rarer events than in high accretors; thus, occurrence, and identification, of one in any of these systems appears to be, unfortunately, highly unlikely, unless many more such systems are discovered. XTE J1701–462 is the exception within this sample, as it exhibited an outburst very similar to MAXI J0556–332’s first observed outburst, while its neutron star exited it with a much lower surface temperature of the order of 150 eV. It may need many more such outbursts until a hyperburst is triggered.

Finally, after this work was completed, our attention was drawn to the work of Suleiman et al. (2022), who studied hybrid crusts (Wijnands et al. 2013), i.e., the conversion of the crust of a neutron star made of catalyzed matter into one of accreted matter during the early phases of accretion. These authors found that as a result of electron captures and the induced changes in density to maintain pressure equilibrium, it is possible to find adjacent layers that present a density inversion, a situation that can develop a Rayleigh–Taylor instability as previously described by Blaes et al. (1990). Suleiman et al. (2022) showed that strong enough density inversions appear several times, during the initial accretion, at densities $\sim 10^{11}$ g cm $^{-3}$ and that the swapping of layers can generate each time $\sim 10^{44}$ ergs. Taken at face value, this mechanism is a good candidate for a hyperburst! Once the outer crust has been completely replaced by accreted matter, such density inversions no longer develop, and thus this interpretation would imply that mass transfer and accretion in the MAXI J0556–332 system was initiated very recently, at most a few millennia ago. Thus, this mechanism appears to be a much less probable explanation of the MAXI J0556–332 neutron star high temperature than a thermonuclear explosion but cannot be a priori excluded.

8. Conclusions

We have shown that the highly anomalous thermal evolution of the MAXI J0556–332 neutron star when exiting its 2011–2012 accretion outburst and during the following years can be very well modeled as being due to the occurrence of a hyperburst, i.e., an explosive nuclear burning of some neutron-rich isotope of O or Ne in a region of density $\sim 10^{11}$ g cm $^{-3}$. Such a deep explosion, depositing $\sim 10^{44}$ ergs, results in a hot outer crust whose cooling takes several years and provides an excellent fit to the data. Published models of nuclear (either stable or explosive) burning during accretion show that the subsistence of a small amount (a few percent in mass fraction) of the needed low Z nuclei to these densities is likely. However, it takes many centuries of accretion to accumulate this material in transient systems, and hyperbursts as postulated here are, thus, very rare events. We are unlikely, unfortunately, to witness another one.

Our complementary results (that modeling of the cooling of the neutron star after the subsequent three accretion outbursts, in 2012, 2015–2016, and 2020 can be realized employing a single parameterization of the still enigmatic shallow heating) lead to a prediction about the future cooling of the neutron star, which will be monitored in the coming years. The example presented in Figure 6 shows a future smooth evolution (see the

“Post-outburst 4” panel) for at least 1000 days, and the 3σ range deduced from our scenario “C” MCMC run (containing more than 4 million cooling curves) shows that this simple behavior is a strong prediction of the scenario.

In the global modeling of 12 yr of evolution of MAXI J0556–332 in our scenario “C” with the hyperburst occurring at the end of the first outburst, parameters describing the shallow heating during this outburst were also assumed to have identical values as in the next three outbursts. We can, hence, describe the whole evolution of the MAXI J0556–332 neutron star during a period of 12 yr through four very different accretion outbursts with a single consistent parameterization of the shallow heating. This result is in agreement with the study of the MXB 1659–29 neutron star that could describe its evolution through two accretion outbursts, spanning a period of almost two decades (1999 until 2018), also with a single shallow heating parameterization (Parikh et al. 2019). These results are, however, in contrast with the modeling of the evolution of the Aquila X-1 neutron star, which exhibits frequent but short accretion outbursts, which required a variation of the shallow heating parameters between different outbursts (Degenaar et al. 2019).

We would like to thank the NICER and Swift teams for approving and executing the observations made during and after the 2020 outburst. D.P. and M.B. acknowledge financial support from the Mexican Consejo Nacional de Ciencia y Tecnología with a CB-2014-1 grant No. 240512 and the Universidad Nacional Autónoma de México through an UNAM-PAPIIT grant No. 109520. M.B. also acknowledges support from a postdoctoral fellowship from UNAM-DGAPA and support from a grant of the Ministry of Research, Innovation and Digitization, CNCS/CCCDI—UEFISCDI, project No. PN-III-P4-ID-PCE-2020-0293, within PNCDI III. J.H. acknowledges financial support from NASA grant 80NSSC19K1611. This research has made use of data and/or software provided by the High Energy Astrophysics Science Archive Research Center (HEASARC), which is a service of the Astrophysics Science Division at NASA/GSFC. This work made use of data supplied by the UK Swift Science Data Centre at the University of Leicester. The authors also benefited from many events organized by the Joint Institute for Nuclear Astrophysics – Center for the Evolution of the Elements (JINA-CEE) and the National Institute for Nuclear Theory (INT) at the University of Washington. We finally thank A. Cumming for pointing to us the work of Suleiman et al. (2022) and the anonymous referee whose constructive comments helped us to improve the paper.

Facilities: CXO, NICER, Swift, XMM-Newton.

Software: NSCool (Page 2016), Numpy (Harris et al. 2020), Matplotlib (Hunter 2007), HEASOFT (NASA/HEASARC 2014), XMM SAS.

Appendix A

Some Details on the Crust Physics We Employ

We take the equation of state and chemical composition of the crust from Haensel & Zdunik (2008) for the model assuming ^{56}Fe at low densities, and fix the crust–core transition density at $\rho_{\text{cc}} \approx 1.5 \times 10^{14}$ g cm $^{-3}$. Reasonable variation of this transition density is known to have very little effect on the crust relaxation modeling (Lalit et al. 2019).

The specific heat is obtained by adding the contribution of the degenerate gas of electrons, the degenerate gas of dripped neutrons in the inner crust, and the nuclei, including the Coulomb interaction contribution in the liquid phase from Slattery et al. (1982) and in the solid phase from Baiko et al. (2001) with a liquid-solid phase transition occurring at a Coulomb coupling parameter $\Gamma = 180$. The only strong interaction modifications to the neutron specific heat we include are from the effect of pairing, for which we follow Levenfish & Yakovlev (1994), while the pairing phase transition critical temperature is taken from Schwenk et al. (2003).

For the thermal conductivity, dominated by electrons, we follow Potekhin et al. (1999) and Gnedin et al. (2001) for electron-phonon scattering in the solid phase, to which we add electron-impurity scattering following the simple treatment of Yakovlev & Urpin (1980). When ions are in the liquid phase, we apply the results of Yakovlev & Urpin (1980). We neglect the very small contribution of electron–electron scattering (Shternin & Yakovlev 2006). We also neglect heat transport from neutrons in the inner crust, which is a very minor contribution (Schmitt & Shternin 2018).

In a very hot crust, as in MAXI J0556–332, neutrino emission from plasmon decay can become a significant sink of energy, and we employ the result of Itoh et al. (1996). We also include neutrino emission from pair annihilation from the same authors, a process that may contribute in cases of extremely hot outer crusts. For the small contribution of electron–ion bremsstrahlung, we follow Kaminker et al. (1999), and we also include neutrino emission for the Cooper breaking and formation process in 1S_0 neutron superfluid phase transition in the inner crust following the treatment described in Page et al. (2009). We do not include neutrino emission from the Urca cycles (Schatz et al. 2014), which may have a significant effect (Deibel et al. 2015) but would force us to introduce more parameters in our MCMC runs to explore the variations in chemical composition that control it.

Our handling of the heating, both from deep crustal heating and shallow heating, and the thermonuclear explosion were described in Section 3. We neglect the effect of nuclear burning in the envelope after the accretion phase, in the form of diffusive nuclear burning, as it has only a small effect for a few days (Wijngaarden et al. 2020).

We do not focus on the physics of the stellar core in the present work, and we simply follow the minimal scenario as described in Page et al. (2004) with no pairing taken into account.

Appendix B Some Details of Our Monte Carlo Runs

Our priors for the distributions of the MCMC parameters are as follows. For the mass M and radius R of the neutron stars, we limit the range of the former from 1.2 to $2.4 M_\odot$ and of the latter from 8 to 16 km with a joint probability distribution in these ranges that is displayed in Figure 13. This distribution encompasses the deduced posteriors from the two classes of models, “PP” and “CS,” of Raaijmakers et al. (2021). The initial, redshifted core temperature \tilde{T}_0 is taken as uniformly distributed in the range $(0.1\text{--}1.5) \times 10^8$ K. About the column density of light elements in the envelope, y_L , measured in g cm^{-2} , we assume a uniform distribution of $\log_{10} y_L$ in the range 6–10, and choose it independently at the beginning of each

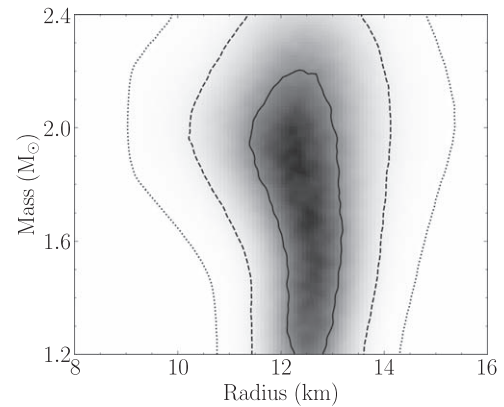


Figure 13. Our prior for the mass and radius distribution. The three contours, continuous, dashed, and dotted, show the 1σ , 2σ , and 3σ ranges, respectively.

accretion outburst, thus having four values $y_L(k)$, $k = 1, \dots, 4$. The resulting $\tilde{T}_0 - T_{\text{eff}}^\infty$ relationship is illustrated in the right panel of Figure 3 in Degenaar et al. (2017). Our next set of parameters comprises the impurity parameters, Q_{imp} , and we divide the crust into five density ranges, in g cm^{-3} : $[10^8, 10^{11}]$, $[10^{11}, 10^{12}]$, $[10^{12}, 10^{13}]$, $[10^{13}, 10^{14}]$, and $[10^{14}, \rho_{\text{cc}}]$, with a value $Q_{\text{imp}}^{(i)}$, $i = 1, \dots, 5$ in each range that is uniformly distributed between 0 and 100. The parameterization of the heating, either shallow or from the hyperburst, has been described in the main text in Section 3.

When varying M and R , we recalculate the structure of the crust by integrating the Tolman-Oppenheimer-Volkoff equation of hydrostatic equilibrium from the outer boundary at $\rho = \rho_b = 10^8 \text{ g cm}^{-3}$ and radius $r = R$ inward until we reach the crust–core density ρ_{cc} , thus giving us the core’s mass and radius, m_c and r_c . This procedure gives us a self-consistent structure of the crust. In this work, we are not interested in the response of the core but still need to define its density and chemical composition profile to employ NSC001. For this purpose, we start with a core structure calculated using the APR EOS (Akmal et al. 1998) and a stellar mass of $1.4 M_\odot$ (that has a core mass $m_c^{(1.4)} = 1.37 M_\odot$ and radius $r_c^{(1.4)} = 10.6$ km), which gives us the density and mass profiles $\rho = \rho^{(1.4)}(r)$ and $m = m^{(1.4)}(r)$. With this, we homogeneously stretch the core as $r \rightarrow r' = (r_c/r_c^{(1.4)})r$, $\rho(r') = \rho^{(1.4)}(r)$ and $m(r') = (m_c/m_c^{(1.4)})m^{(1.4)}(r)$.

Our MCMC driver MXMX is specially designed to efficiently drive NSC001, and it applies the basic techniques of emcee (Foreman-Mackey et al. 2013). It can handle arbitrary numbers of walkers in an arbitrary number of tempered chains, moving either in individual random walks or in affine invariant stretches (Christen 2007; Goodman & Weare 2010). For the present work, we found the optimal configuration was having five tempered chains, with “temperatures” $T = 1, 2, 5, 10$, and 100, each having 100 walkers. The basic chain applied stretches and the other chains simple walks. After initial burn-in, the chains of scenarios “A” and “B” had more than 2 million points, while that of scenario “C” had more than four million points. We calculated the integrated autocorrelation lengths (Sokal 1997) τ of each parameter of each walker: typical values are 50–100, and the longest ones do not exceed 200 in all three scenarios. We thus have, in each scenario, more than 100 effectively independent samples from each walker.

For completeness, we display in Figure 14 the posterior distributions of the remaining 10 parameters of our scenario

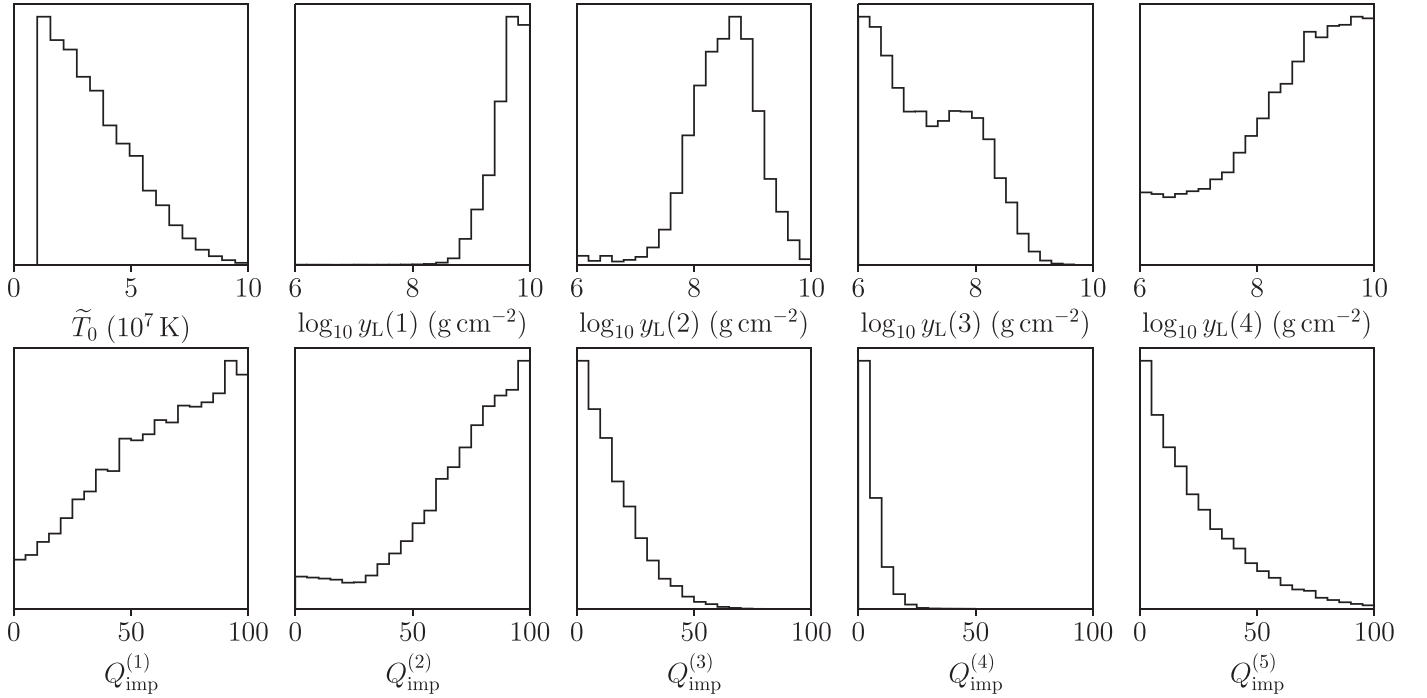


Figure 14. Posterior distribution of the remaining parameters in our scenario “C” that are not displayed in Figures 9 and 10.

“C” MCMC that were not displayed in Figures 9 and 10 for not being crucial to the purpose of this work. Interesting to note are the preference for cold cores, \tilde{T}_0 , and the contrast in the distribution of Q_{imp} in regions 1 and 2, i.e., essentially below neutron drip, versus regions 3, 4, and 5, i.e., above neutron drip. One expects a hyperburst to significantly reduce the impurity content, as all low Z nuclei are burned into iron-peak nuclei while the MCMC prefers high impurity in the region (1), i.e., at densities below $10^{11} \text{ g cm}^{-3}$, precisely where the hyperburst happened (and in region (2) whose matter should have also been processed by previous hyperbursts). However, low Q_{imp} are *not excluded* in regions (1) and (2), only disfavored, and low Q_{imp} values actually just favor a thick crust, i.e., not too high neutron star masses and not too small radii. There is, thus, nothing contradictory, nor conclusive, in these impurity content posteriors. They would favor the secondary peak, low M and large R , in the M and R distributions discussed in Section 5, if one added the new prior that the hyperburst would result in low Q_{imp} , at least in region 1. (For this reason, we choose our illustrative model for Figures 6 and 7 as a $1.6 M_{\odot}$ star with an 11.2 km radius.)

Appendix C Electron Captures on α -Nuclei

For studying electron captures, we have followed the scheme of Sato (1979) and Haensel & Zdunik (1990). We choose an initial nucleus (Z, N) , $N = A - Z$ as the neutron number of the nucleus, and follow its evolution as pressure is increased. We only consider α nuclei, i.e., Z is even and $N = Z$. When reaching a critical point where the electron chemical potential μ_e is large enough, an initial electron capture occurs, resulting in an odd–odd nucleus $(Z - 1, N + 1)$ at which point, due to pairing, a second electron capture immediately happens leading to an even–even nucleus $(Z - 2, N + 2)$. The criterion for the

first electron capture is that

$$\begin{aligned} W_N(Z, N) + W_C(Z, n_e) + \mu_e(n_e) \\ = W_N(Z - 1, N + 1) + W_C(Z - 1, n_e) \end{aligned} \quad (\text{C1})$$

where $W_N(Z, N) = M_N(Z, N)c^2$ is the energy, M_N is its mass of the nucleus (Z, N) , $W_C(Z, n_e)$ is the Coulomb energy of the nucleus’ Wigner-Seitz cell immersed in a medium with electron density n_e , and μ_e is the electron chemical potential. For the Coulomb energy, we apply the ion sphere value $W_C(Z, n_e) = -0.9Z^{5/3}e^2/a_e$ where e is the elementary charge unit and $a_e \equiv (3/4\pi n_e)^{1/3}$ (Shapiro & Teukolsky 1983). We deduce $M_N(Z, N)$ from the atomic mass $M_{\text{atom}}(Z, N)$ of the AME2020 table (Wang et al. 2021) as $M_N(Z, N) = M_{\text{atom}}(Z, N) - Zm_e + B_{\text{el}}$ where m_e is the electron mass and the electrons binding energy is approximated as $B_{\text{el}} = 14.4381 Z^{2.39} + 1.55468 \times 10^{-6} Z^{5.35} \text{ eV}$ (Lunney et al. 2003). We then keep increasing the pressure looking for further electron captures leading to $(Z - 4, N + 4)$, and so on, until the neutron drip point is reached. The resulting evolutions are presented in Figure 11.

Appendix D Nuclear Fusion Processes and Screening

We consider nuclei of charge and mass numbers Z_i and A_i and mass M_i undergoing a fusion reaction $(A_1, Z_1) + (A_2, Z_2) \rightarrow (A_c, Z_c)$. For this we need to know the fusion cross section σ and calculate the fusion rate including a proper treatment of plasma screening. The cross section is commonly expressed as

$$\sigma(E) = \frac{S(E)}{E} \exp(-2\pi\eta) \quad (\text{D1})$$

where $S(E)$ is the “astrophysical S-factor,” E is the center of mass energy, and $\eta = Z_1 Z_2 e^2 / \hbar v$ is the Gamow parameter,

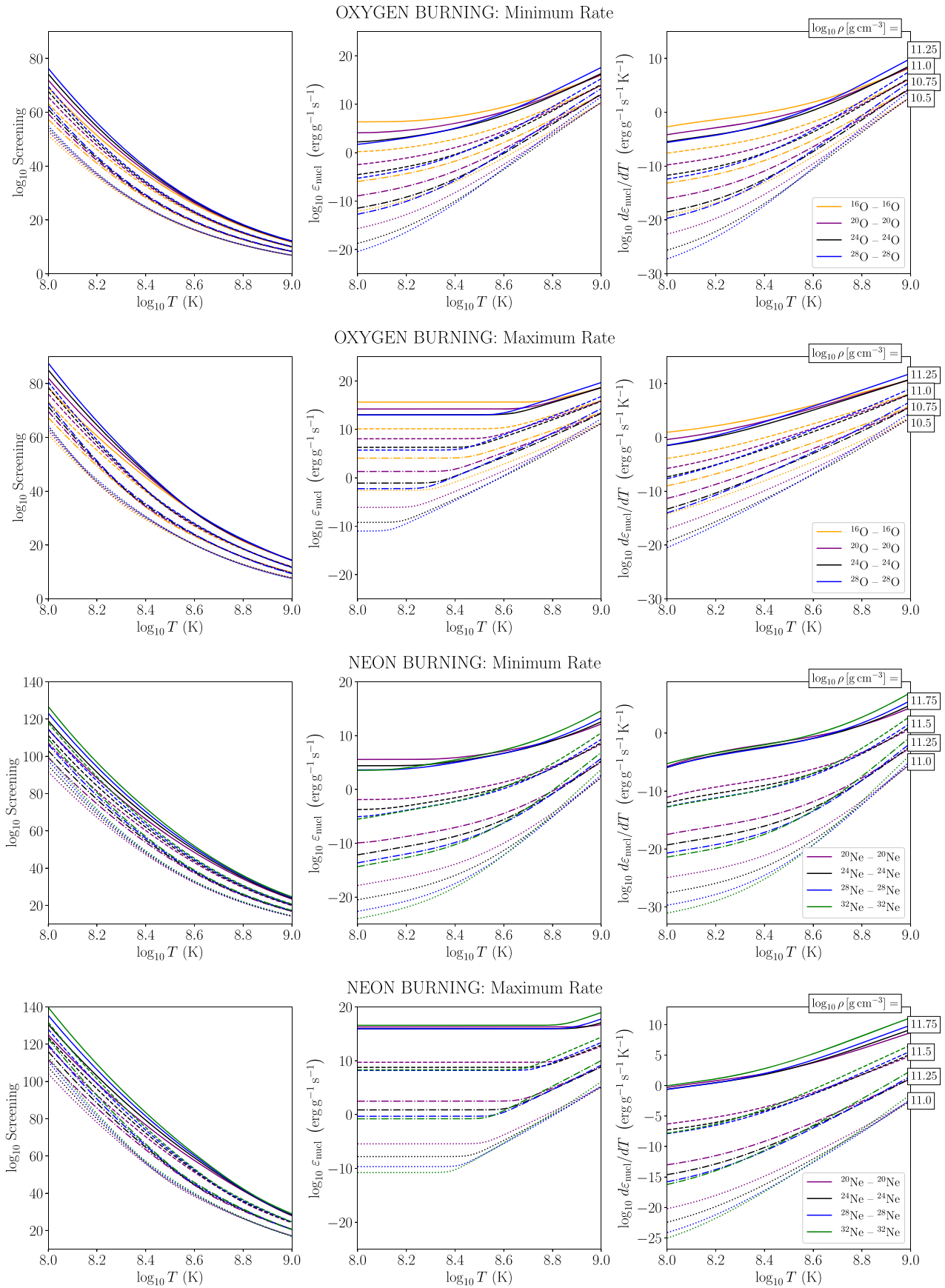


Figure 15. Screening factors, energy generation rates, ϵ_{nucl} , and their temperature sensitivity, $d\epsilon_{\text{nucl}}/dT$, for fusions of several isotopes of oxygen (upper panels) and neon (lower panels) at chosen densities. We used both the “minimum” and “maximum” reaction rates as labeled in the panel headings. In all cases, we assumed a mass fraction $X = 10^{-3}$ within a background of ^{56}Ca .

where $v = \sqrt{2E/\mu}$ is the relative velocity, and $\mu = M_1 M_2 / (M_1 + M_2)$ is the reduced mass. For our purpose, we need an extended set of fusion reactions involving neutron-rich nuclei, and we employ the results of Afanasjev et al. (2012), which provide a consistent scheme covering thousands of possible reactions. These authors calculated $S(E)$ using the São Paulo potential with the barrier penetration formalism (SP-BP; Chamon et al. 2002; Gasques et al. 2005) and provided simple analytical fits to their results.

In the purely thermonuclear regime, i.e., at high temperatures where screening can be neglected, the fusion rate is given by the standard result (e.g., Kippenhahn et al. 2012)

$$R = \frac{n_1 n_2}{1 + \delta_{12}} S(E^{\text{pk}}) \frac{r_B}{\hbar} P F \quad (\text{D2})$$





where n_i is the number density of nucleus i , $r_B = \hbar^2 / (2\mu Z_1 Z_2 e^2)$, and $S(E)$ is evaluated at the Gamow peak energy $E^{\text{pk}} = (\pi k_B T / 2)^{2/3} E_a^{1/3}$ with $E_a = Z_1 Z_2 e^2 / r_B$. $F = \exp[-\tau]$ describes the Coulomb barrier penetration with $\tau = 3E^{\text{pk}} / k_B T$ and the prefactor $P = 16\tau^2 / (3^{5/2} \pi)$. (The $1 + \delta_{12}$ term avoids double counting in the case that nuclei 1 and 2 are identical).

Based on their previous work (Gasques et al. 2007), Afanasjev et al. (2012) stated that typical uncertainties on their $S(E)$ calculations are of the order of two to four for stable nuclei but can be about a factor 10 in the cases of neutron-rich nuclei and even up to 100 at low energies. For example, in the case of the three typical fusion reactions of $^{12}\text{C}+^{12}\text{C}$, $^{12}\text{C}+^{16}\text{O}$, and $^{16}\text{O}+^{16}\text{O}$, we find that the thermonuclear rates from Equation (D2) using $S(E)$ from Afanasjev et al. (2012) can be up to four to five times smaller than the classical values from Caughlan & Fowler (1988). For another comparison, including important cases of reactions with no experimental measurements, Umar et al. (2012) performed dynamical density-constrained time dependent Hartree–Fock (DC-TDHF) calculations of $S(E)$ for several C and O reactions and compared them to the static SP-BP results. In the cases of $^{12}\text{C}+^{16}\text{O}$ and $^{16}\text{O}+^{16}\text{O}$, they obtained excellent agreement with experimental values for the DC-TDHF results (while the SP-BP results are about four times smaller, as seen above). In the cases of $^{12}\text{C}+^{24}\text{O}$ and $^{16}\text{O}+^{24}\text{O}$, they found that the SP-BP results are also smaller than the DC-TDHF ones, by about one order of magnitude, while in the case of the $^{24}\text{O}+^{24}\text{O}$, the situation reversed with SP-BP values being larger than DC-TDHF ones. (No experimental values are available for these last three reactions.) As seen below, variations of even a factor 10 in $S(E)$ have very little impact on our results. Notice that resonances are not included in any of these models that only provide an average $S(E)$, but their effect is small as long as their width is much smaller than the width of the Gamow peak (Yakovlev et al. 2006).

The second ingredient needed to calculate realistic fusion rates in the dense medium of the neutron star crust is proper inclusion of the screening of the Coulomb repulsion. In our cases, this effect increases the rates by *many tens* of orders of magnitude. We employ the treatment proposed by Gasques et al. (2005) and Yakovlev et al. (2006), which allows to cover the whole range from the $T = 0$ pycnonuclear regime up to the thermonuclear one by adjusting E^{pk} and appropriately modifying the two functions P and F in Equation (D2). In the thermonuclear regime, screening can be accurately incorporated while in the opposite pycnonuclear regime, uncertainties are enormous, possibly up to 10 orders of magnitude. We will apply the two cases of Yakovlev et al. (2006) that give

expected minimal and maximal screening effects to hopefully bracket the unknown correct value. From the rate per unit volume R , one deduces the energy generation rate, per unit mass, $\varepsilon_{\text{nucl}} = QR/\rho$ where Q is the energy released per reaction. Relevant screening factors, energy generation rates $\varepsilon_{\text{nucl}}$, and their temperature sensitivity $d\varepsilon_{\text{nucl}}/dT$ are plotted in Figure 15. The flat portion of the $\varepsilon_{\text{nucl}}$ curve exhibits the pycnonuclear regime, and comparison with Figure 12 shows that the triggering of the hyperburst occurred in the regime of transition from purely pycnonuclear to thermonuclear.

ORCID iDs

Dany Page  <https://orcid.org/0000-0003-2498-4326>
 Jeroen Homan  <https://orcid.org/0000-0001-8371-2713>
 Martin Nava-Callejas  <https://orcid.org/0000-0003-2334-6947>
 Yuri Cavecchi  <https://orcid.org/0000-0002-6447-3603>
 Mikhail V. Beznogov  <https://orcid.org/0000-0002-7326-7270>
 Nathalie Degenaar  <https://orcid.org/0000-0002-0092-3548>
 Rudy Wijnands  <https://orcid.org/0000-0002-3516-2152>

References

- Afanasjev, A. V., Beard, M., Chugunov, A. I., Wiescher, M., & Yakovlev, D. G. 2012, *PhRvC*, **85**, 054615
- Akmal, A., Pandharipande, V. R., & Ravenhall, D. G. 1998, *PhRvC*, **58**, 1804
- Arnaud, K. A. 1996, in ASP Conf. Ser. 101, *Astronomical Data Analysis Software and Systems V*, ed. G. H. Jacoby & J. Barnes (San Francisco, CA: ASP), 17
- Baiko, D. A., Potekhin, A. Y., & Yakovlev, D. G. 2001, *PhRvE*, **64**, 057402
- Beznogov, M. V., Page, D., & Ramirez-Ruiz, E. 2020, *ApJ*, **888**, 97
- Bildsten, L., Buccheri, R., van Paradijs, J., & Alpar, A. 1998, in ASIC Conf. Ser. 515, *The Many Faces of Neutron Stars*, ed. R. Buccheri, J. van Paradijs, & M. A. Alpar (Dordrecht: Kluwer), 419
- Bisnovatyi-Kogan, G. S., & Chechetkin, V. M. 1979, *SvPhU*, **22**, 89
- Blaes, O., Blandford, R., Madau, P., & Koonin, S. 1990, *ApJ*, **363**, 612
- Brown, E. F., Bildsten, L., & Rutledge, R. E. 1998, *ApJL*, **504**, L95
- Brown, E. F., & Cumming, A. 2009, *ApJ*, **698**, 1020
- Burrows, D. N., Hill, J. E., Nousek, J. A., et al. 2005, *SSRv*, **120**, 165
- Cackett, E. M., Wijnands, R., Linares, M., et al. 2006, *MNRAS*, **372**, 479
- Caughlan, G. R., & Fowler, W. A. 1988, *ADNDT*, **40**, 283
- Chamon, L. C., Carlson, B. V., Gasques, L. R., et al. 2002, *PhRvC*, **66**, 014610
- Christen, J. 2007, A General Purpose Scale-Independent MCMC Algorithm, Centro de Investigación en Matemáticas, Guanajuato Technical Report, I-07-16, <https://ciimat.repositorioinstitucional.mx/jspui/bitstream/1008/645/1/I-07-16.pdf>
- Colpi, M., Geppert, U., Page, D., & Possenti, A. 2001, *ApJL*, **548**, L175
- Cumming, A., & Bildsten, L. 2001, *ApJL*, **559**, L127
- Cumming, A., Macbeth, J., in't Zand, J. J. M., & Page, D. 2006, *ApJ*, **646**, 429
- Cybur, R. H., Amthor, A. M., Heger, A., et al. 2016, *ApJ*, **830**, 55
- Degenaar, N., Ootes, L. S., Page, D., et al. 2019, *MNRAS*, **488**, 4477
- Degenaar, N., Ootes, L. S., Reynolds, M. T., Wijnands, R., & Page, D. 2017, *MNRAS*, **465**, L10
- Degenaar, N., Page, D., van den Eijnden, J., et al. 2021, *MNRAS*, **508**, 882
- Degenaar, N., Wijnands, R., Bahramian, A., et al. 2015, *MNRAS*, **451**, 2071
- Deibel, A., Cumming, A., Brown, E. F., & Page, D. 2015, *ApJL*, **809**, L31
- Evans, P. A., Beardmore, A. P., Page, K. L., et al. 2007, *A&A*, **469**, 379
- Evans, P. A., Beardmore, A. P., Page, K. L., et al. 2009, *MNRAS*, **397**, 1177
- Fantina, A. F., Zdunik, J. L., Chamel, N., et al. 2018, *A&A*, **620**, A105
- Foreman-Mackey, D., Hogg, D. W., Lang, D., & Goodman, J. 2013, *PASP*, **125**, 306
- Fridriksson, J. K., Homan, J., & Remillard, R. A. 2015, *ApJ*, **809**, 52
- Fridriksson, J. K., Homan, J., Wijnands, R., et al. 2010, *ApJ*, **714**, 270
- Fujimoto, M. Y., Hanawa, T., & Miyaji, S. 1981, *ApJ*, **247**, 267
- Fushiki, I., & Lamb, D. Q. 1987, *ApJL*, **323**, L55
- Galloway, D. K., & Keek, L. 2021, in *Timing Neutron Stars: Pulsations, Oscillations and Explosions*, ed. T. M. Belloni, M. Méndez, & C. Zhang, Vol. 461 (Berlin: Springer), 209
- Gasques, L. R., Afanasjev, A. V., Aguilera, E. F., et al. 2005, *PhRvC*, **72**, 025806
- Gasques, L. R., Afanasjev, A. V., Beard, M., et al. 2007, *PhRvC*, **76**, 045802

- Gendreau, K. C., Arzoumanian, Z., Adkins, P. W., et al. 2016, *Proc. SPIE*, **9905**, 99051H
- Gnedin, O. Y., Yakovlev, D. G., & Potekhin, A. Y. 2001, *MNRAS*, **324**, 725
- Goodman, J., & Weare, J. 2010, *CAMCS*, **5**, 65
- Gupta, S. S., Kawano, T., & Möller, P. 2008, *PhRvL*, **101**, 231101
- Haensel, P., & Zdunik, J. L. 1990, *A&A*, **227**, 431
- Haensel, P., & Zdunik, J. L. 2008, *A&A*, **480**, 459
- Harris, C. R., Millman, K. J., van der Walt, S. J., et al. 2020, *Natur*, **585**, 357
- Hasinger, G., & van der Klis, M. 1989, *A&A*, **225**, 79
- Heinke, C., Rybicki, G., Narayan, R., & Grindlay, J. 2006, *ApJ*, **644**, 1090
- Homan, J., Fridriksson, J. K., Wijnands, R., et al. 2014, *ApJ*, **795**, 131
- Homan, J., Linares, M., van den Berg, M., & Fridriksson, J. 2011, *ATel*, **3650**, 1
- Horowitz, C. J., Berry, D. K., & Brown, E. F. 2007, *PhRvE*, **75**, 066101
- Hunter, J. D. 2007, *CSE*, **9**, 90
- Itoh, N., Hayashi, H., Nishikawa, A., & Kohyama, Y. 1996, *ApJS*, **102**, 411
- Kaminker, A. D., Pethick, C. J., Potekhin, A. Y., Thorsson, V., & Yakovlev, D. G. 1999, *A&A*, **343**, 1009
- Kaspi, V. M., & Beloborodov, A. M. 2017, *ARA&A*, **55**, 261
- Keek, L., & Heger, A. 2011, *ApJ*, **743**, 189
- Kippenhahn, R., Weigert, A., & Weiss, A. 2012, *Stellar Structure and Evolution* (Berlin: Springer)
- Kuulkers, E., den Hartog, P. R., in 't Zand, J. J. M., et al. 2003, *A&A*, **399**, 663
- Lalit, S., Meisel, Z., & Brown, E. F. 2019, *ApJ*, **882**, 91
- Lau, R., Beard, M., Gupta, S. S., et al. 2018, *ApJ*, **859**, 62
- Levenfish, K. P., & Yakovlev, D. G. 1994, *ARep*, **38**, 247
- Lin, D., Altamirano, D., Homan, J., et al. 2009, *ApJ*, **699**, 60
- Lin, D., Remillard, R. A., & Homan, J. 2007, *ApJ*, **667**, 1073
- Lin, D., Strader, J., Carrasco, E. R., et al. 2018, *NatAs*, **2**, 656
- Lunney, D., Pearson, J. M., & Thibault, C. 2003, *RvMP*, **75**, 1021
- Matsumura, T., Negoro, H., Suwa, F., et al. 2011, *ATel*, **3102**, 1
- Merritt, R. L., Cackett, E. M., Brown, E. F., et al. 2016, *ApJ*, **833**, 186
- Miralda-Escude, J., Haensel, P., & Paczynski, B. 1990, *ApJ*, **362**, 572
- NASA/HEASARC 2014, HEASoft: Unified Release of FTOOLS and XANADU, Astrophysics Source Code Library, ascl:1408.004, <https://heasarc.gsfc.nasa.gov/lheasoft/>
- Negoro, H., Yoshitake, T., Nakajima, M., et al. 2020, *ATel*, **13628**, 1
- Ootes, L. S., Page, D., Wijnands, R., & Degenaar, N. 2016, *MNRAS*, **461**, 4400
- Ootes, L. S., Wijnands, R., Page, D., & Degenaar, N. 2018, *MNRAS*, **477**, 2900
- Ootes, L. S., Vats, S., Page, D., et al. 2019, *MNRAS*, **487**, 1447
- Page, D. 2016, NSCool: Neutron star cooling code, Astrophysics Source Code Library, ascl:1609.009, <https://www.astroscu.unam.mx/neutrones/NSCool/>
- Page, D., Lattimer, J. M., Prakash, M., & Steiner, A. W. 2004, *ApJS*, **155**, 623
- Page, D., Lattimer, J. M., Prakash, M., & Steiner, A. W. 2009, *ApJ*, **707**, 1131
- Page, D., & Reddy, S. 2013, *PhRvL*, **111**, 241102
- Parikh, A. S., Homan, J., Wijnands, R., et al. 2017a, *ApJL*, **851**, L28
- Parikh, A. S., Wijnands, R., Degenaar, N., et al. 2017b, *MNRAS*, **466**, 4074
- Parikh, A. S., Wijnands, R., Degenaar, N., Ootes, L., & Page, D. 2018, *MNRAS*, **476**, 2230
- Parikh, A. S., Wijnands, R., Homan, J., et al. 2020, *A&A*, **638**, L2
- Parikh, A. S., Wijnands, R., Ootes, L. S., et al. 2019, *A&A*, **624**, A84
- Potekhin, A. Y., Baiko, D. A., Haensel, P., & Yakovlev, D. G. 1999, *A&A*, **346**, 345
- Potekhin, A. Y., & Chabrier, G. 2012, *A&A*, **538**, A115
- Raaijmakers, G., Greif, S. K., Hebeler, K., et al. 2021, *ApJL*, **918**, L29
- Remillard, R. A., Loewenstein, M., Steiner, J. F., et al. 2022, *AJ*, **163**, 130
- Rutledge, R., Bildsten, L., Brown, E., et al. 2002, *ApJ*, **580**, 413
- Sato, K. 1979, *PhThPh*, **62**, 957
- Schatz, H., Aprahamian, A., Barnard, V., et al. 2001, *PhRvL*, **86**, 3471
- Schatz, H., Bildsten, L., Cumming, A., & Wiescher, M. 1999, *ApJ*, **524**, 1014
- Schatz, H., Gupta, S., Möller, P., et al. 2014, *Natur*, **505**, 62
- Schmitt, A., & Shternin, P. 2018, in *The Physics and Astrophysics of Neutron Stars*, ed. L. Rezzolla et al., Vol. 457 (Cham: Springer), 455
- Schwenk, A., Friman, B., & Brown, G. E. 2003, *NuPhA*, **713**, 191
- Shapiro, S. L., & Teukolsky, S. A. 1983, *Black Holes, White Dwarfs and Neutron Stars: The Physics of Compact Objects* (New York: Wiley)
- Shechtilin, N. N., Gusakov, M. E., & Chugunov, A. I. 2021, *MNRAS*, **507**, 3860
- Shternin, P. S., & Yakovlev, D. G. 2006, *PhRvD*, **74**, 043004
- Shternin, P. S., Yakovlev, D. G., Haensel, P., & Potekhin, A. Y. 2007, *MNRAS*, **382**, L43
- Slattery, W. L., Doolen, G. D., & Dewitt, H. E. 1982, *PhRvA*, **26**, 2255
- Sokal, A. 1997, in *Functional Integration*, ed. C. DeWitt-Morette, P. Cartier, & A. Folacci, Vol. 361 (Boston, MA: Springer), 131
- Suleiman, L., Zdunik, J.-L., Haensel, P., & Fortin, M. 2022, *A&A*, **662**, A63
- Umar, A. S., Oberacker, V. E., & Horowitz, C. J. 2012, *PhRvC*, **85**, 055801
- Wallace, R. K., & Woosley, S. E. 1981, *ApJS*, **45**, 389
- Wang, M., Huang, W., Kondev, F., Audi, G., & Naimi, S. 2021, *ChPhC*, **45**, 030003
- Waterhouse, A. C., Degenaar, N., Wijnands, R., et al. 2016, *MNRAS*, **456**, 4001
- Wijnands, R., Degenaar, N., & Page, D. 2013, *MNRAS*, **432**, 2366
- Wijnands, R., Miller, J. M., Markwardt, C., Lewin, W. H. G., & van der Klis, M. 2001, *ApJL*, **560**, L159
- Wijngaarden, M. J. P., Ho, W. C. G., Chang, P., et al. 2020, *MNRAS*, **493**, 4936
- Yakovlev, D. G., Gasques, L. R., Afanasjev, A. V., Beard, M., & Wiescher, M. 2006, *PhRvC*, **74**, 035803
- Yakovlev, D. G., & Urpin, V. A. 1980, *SvA*, **24**, 303